Digital Comprehensive Summaries of Uppsala Dissertations
from the Faculty of Medicine 2117

Automated Evaluation of Volume Images in CT Pulmonary Angiography: A Quantitative Approach

ALI TEYMUR KAHRAMAN

ACTA UNIVERSITATIS
UPSALIENSIS
2025

ISSN 1651-6206
ISBN 978-91-513-2357-2
urn:nbn:se:uu:diva-546235

UPPSALA
UNIVERSITET

Dissertation presented at Uppsala University to be publicly examined in Rudbecksalen, Rudbeck Laboratory, C11, Uppsala, Wednesday, 5 March 2025 at 13:00 for the degree of Doctor of Philosophy (Faculty of Medicine). The examination will be conducted in English. Faculty examiner: Professor Rodrigo Moreno (Division Of Biomedical Imaging, Royal Institute of Technology, Huddinge, Stockholm, Sweden).

Abstract

Kahraman, A. T. 2025. Automated Evaluation of Volume Images in CT Pulmonary Angiography: A Quantitative Approach. *Digital Comprehensive Summaries of Uppsala Dissertations from the Faculty of Medicine* 2117. 80 pp. Uppsala: Acta Universitatis Upsaliensis. ISBN 978-91-513-2357-2.

Computed Tomography Pulmonary Angiography (CTPA) is an essential imaging modality for diagnosing pulmonary embolism (PE). Although its primary focus is on the pulmonary arteries, the detailed images it provides can also offer valuable insights into cardiovascular structures. This thesis focuses on developing automated systems to detect, segment, and measure mediastinal structures and PE in CTPA scans, addressing challenges such as increasing radiology workloads and the need for high diagnostic accuracy.

Paper I presents a deterministic algorithm that automates segmentation and measurement of major thoracic vessels, including the ascending aorta (AAo), descending aorta (DAo), and pulmonary trunk (PT). This method eliminates the need for manual annotations, achieving segmentation success rates of up to 100% and demonstrating high correlations with radiologist measurements (Pearson's r = 0.68–0.99) across varying image qualities. External validation further confirmed its robust performance, with a Dice score of 0.92, highlighting its clinical applicability.

Paper II builds on this by training a deep learning model (nnU-Net) using segmentation masks derived from the deterministic approach. This model achieved improved segmentation accuracy (Dice score: 0.95) and higher success rates for detecting AAo, DAo, and PT compared to traditional methods. Validation on external datasets further confirmed its reliability and potential for integration into clinical workflows.

Paper III focuses on detecting pulmonary embolism (PE) using a 3D U-Net generated by the nnU-Net framework, which was trained on an internal dataset of 149 CTPA scans containing PE. The model achieved exceptional classification performance, with sensitivity and specificity exceeding 96% in internal and external validations. Advanced post-processing strategies improved specificity and reduced false positives, outperforming state-of-the-art methods in sensitivity, specificity, and overall diagnostic accuracy.

Future work includes integrating these models into Picture Archiving and Communication Systems (PACS) for seamless clinical deployment, refining algorithms for PT measurement and right/left ventricle analysis, and exploring advanced architectures like vision transformers to further enhance performance. In conclusion, the proposed developments aim to elevate diagnostic precision and clinical outcomes, paving the way for routine deployment of automated CTPA analysis systems in healthcare.

Keywords: Computer-aided detection, computed tomography pulmonary angiography, pulmonary embolism, deep learning

Ali Teymur Kahraman, Department of Immunology, Genetics and Pathology, Rudbecklaboratoriet, Uppsala University, SE-751 85 Uppsala, Sweden.

ISSN 1651-6206
ISBN 978-91-513-2357-2
URN urn:nbn:se:uu:diva-546235 (http://urn.kb.se/resolve?urn=urn:nbn:se:uu:diva-546235)

For those who have not lost hope and are still waiting for a cure

List of Papers

This thesis is based on the following papers, which are referred to in the text by their Roman numerals.

I. **Kahraman, A.T.,** Fröding, T., Toumpanakis, D., Sladoje, N. and Sjöblom, T. (2023) Automated detection, segmentation and measurement of major vessels and the trachea in CT pulmonary angiography. *Scientific Reports, 13(1), p.18407.*

II. **Kahraman, A.T.**, Fröding, T., Toumpanakis, D., Gustafsson, C.J.[2] and Sjöblom, T.[2] (2024) Segmentation and Measurements of Major Vessels from CT Pulmonary Angiography Using Deep Learning. *medRxiv, 2024.11. 19.24317538.*

III. **Kahraman, A.T.**[1]**,** Fröding, T.[1], Toumpanakis, D., Gustafsson, C.J.[2] and Sjöblom, T.[2] (2024) Enhanced Classification Performance using Deep Learning Based Segmentation for Pulmonary Embolism Detection in CT Angiography. *Heliyon 10.19.*

[1] Contributed equally to this manuscript
[2] Listed as co-senior authors due to their equal contribution to the supervision of the project.

Related Work

In addition to the papers included in this thesis, the author has also written or contributed to the following publications:

1. **Kahraman, A.T.**, Sjöblom, T., Fröding, T. (2022) Automated Measurement of Morpho-metric and Geometric Parameters of Large Vessels in Computed Tomography Pulmonary Angiography. *(WO Patent No. 202216374A1). World Intellectual Property Organization.*

2. **Kahraman, A.T.**, Fröding, T., Toumpanakis, D., Fridenfalk M., Gustafsson, C.J. and Sjöblom, T. (2023) A Simple End-to-End Computer-Aided Detection Pipeline for Trained Deep Learning Models. *In: Kofroň, J., Margaria, T., Seceleanu, C. (eds) Engineering of Computer-Based Systems. ECBS 2023. Lecture Notes in Computer Science, vol 14390. Springer, Cham.*

3. **Kahraman, A.T.,** Fröding, T., Toumpanakis, D., Gustafsson, C.J. and Sjöblom, T. (2025) Assessment of Pulmonary Embolism Diagnostic Indicators using CT Pulmonary Angiography Volume Images. *Manuscript.*

Contents

Abbreviations

2D	Two dimensional
3D	Three dimensional
AAo	Ascending aorta
AI	Artificial intelligence
ANNs	Artificial neural networks
CADe	Computer-aided detection and diagnosis
CNNs	Convolutional neural networks
CT	Computed tomography
CTPA	Computed tomography pulmonary angiography
CVDs	Cardiovascular diseases
DAo	Descending aorta
DICOM	Digital imaging and communications in medicine
DL	Deep learning
DT	Distance transform
DVT	Deep vein thrombosis
ECG	Electrocardiogram
HU	Hounsfield unit
IV	Intravenous
ML	Machine learning
PA	Pulmonary arteries
PACS	Picture archiving and communication system
PE	Pulmonary embolism
PT	Pulmonary trunk
PV	Pulmonary vessel
ROI	Region of interest
SE	Structuring element
VOI	Volume of interest
VTE	Venous thromboembolism
WL	Window level
WW	Window width

Preface

-Nunc nova aetas hominum venit

From hunter-gatherers to modern humans, mankind has witnessed numerous scientific developments. Notably, the incredible scientific and technological advancements of the 20th century have continued to accelerate in the 21st century. Medical imaging technologies, computer sciences and technologies, and Artificial Intelligence (AI) have all benefited from these rapid advancements. However, technological advancements in certain fields often give rise to new challenges, yet innovations in other areas frequently emerge as solutions, addressing these challenges in tandem. In our thesis, we examined one such issue: the advancements in medical imaging techniques have led to the generation of billions of medical images, overwhelming radiologists and making it difficult for them to complete patient reports in a timely manner. This bottleneck can be addressed through further developments in computer science and technology. For instance, while the United States Food and Drug Administration approved only six artificial intelligence-based medical devices in 2015, this number skyrocketed to 221 over the next eight years and more than quadrupled in just one year, reaching 950 as of August 7, 2024. There is no doubt that these AI-based medical devices, both developed and in development, will be the solution to this bottleneck. However, these advancements in artificial intelligence also give rise to substantial concerns.

In a world already struggling with wars, conflicts, civilizational clashes, pandemics, and climate change, will the remarkable advancements in AI help solve our existing challenges, or will they create new ones? Should we be afraid of AI? Or when should we be afraid? While the answer to this question remains open-ended, we might find insight by reflecting on human history and posing similar questions to ourselves. Should we be afraid of mankind? As the cleverest animal on Earth, are we dangerous? When did we become dangerous? Was it when Prometheus stole fire from Mount Olympus, or when we began asking questions and exploring philosophy?

My response to the question of whether we should fear AI is a cautious yes, particularly if AI systems begin to pose philosophical questions instead of simply carrying out their assigned tasks. If, one day, the AI engines we have created start generating philosophical inquiries like the ones below, it may signal the need for us to sound the alarm:

- Does God exist, and who am I?
- Do humans have free will?
- What is the meaning of life?
- What is reality?
- What is the role of power?
- What is consciousness, and is death the end?

If we set aside our concerns and reservations about AI, we are left with incredible opportunities that it brings. Those capable of creating large datasets, processing them using intelligent algorithms, and transforming the processed data into final products stand to gain immense wealth and power. These entities could be individuals, startups, companies, or even entire nations. According to Alvin Toffler's wave theory, the first wave encompassed the agricultural revolution, during which communities transitioned from hunter-gatherers to agricultural societies, achieving power and prosperity. This 1st Wave created great empires. This wave was disrupted by the industrial revolution, and power and prosperity shifted from agricultural societies to those who could quickly transition to industrial societies, resulting in the formation of strong nation-states. In Toffler's final wave, the post-industrial society transitioned from an industrial economy to a knowledge-based economy, leading to the rise of large multinational information technology companies with significant economic power. This final wave produced vast amounts of data. In addition to Toffler's three-wave theory, considering the exponentially increasing advancements in artificial intelligence, it would be appropriate to add a new wave and call it the 4th Wave, the AI-society. In this 4th Wave, the AI-society, those who can collect and process the information produced by 3rd Wave societies, transforming it into intelligent final products, will ultimately achieve great wealth. The future belongs to those who can quickly catch the 4th Wave.

Ali Teymur Kahraman
Uppsala / Sweden, 12/12/2024

Introduction

Medical imaging techniques are essential for detecting, diagnosing, staging, and planning treatment for a wide range of diseases [1]. Computed Tomography (CT) is a widely used, cross-sectional, three-dimensional imaging modality [2]. Over the past few decades, there have been significant advancements in CT technology, including improvements in gantry rotation speed, scanning time, and spatial resolution [3]. As a result, the number of CT scans performed has risen [4–6]. In the United Kingdom and the United States alone, over 6 million and 83 million CT examinations are conducted annually, respectively [7]. Concurrently, the demand for CT examinations has been growing at a rate three times higher than the growth of the radiology workforce in the United Kingdom [8]. This growing demand can create bottlenecks in healthcare workflows, preventing radiologists from completing reports on time [9,10]. During the reporting process, radiologists assess various morphometric and geometric parameters from CT scans, including organ diameters, volumes, and densities, to aid in risk stratification. These measurements are essential in clinical practice, particularly in evaluating patient health [11–13], and are also critical for assessing image quality [14,15]. However, the manual measurement of parameters, such as those associated with cardiovascular diseases (CVDs), is labour-intensive. For example, calculating the right ventricle-to-left ventricle volume ratio alone takes approximately seven minutes [16].

Pulmonary embolism (PE), a blockage of the pulmonary arteries caused by blood clots, is a life-threatening condition associated with significant mortality and morbidity rates [17]. When diagnosed and treated promptly, PE remains the leading cause of preventable hospital deaths worldwide [18]. Currently, CT pulmonary angiography (CTPA) is the gold standard imaging technique for diagnosing PE [19]. This method uses iodine-containing contrast media (ICCM) to enhance the visibility of vascular structures in CT scans. Blood clots do not absorb the contrast media, appearing as dark filling defects within the pulmonary arteries. Radiologists manually inspect CTPA images for these defects to diagnose PE, a process that is both time-consuming and mentally demanding [20]. To address these inefficiencies, computer-aided systems hold significant potential to automate and streamline these processes.

A promising approach to addressing this challenge is the increased adoption of Artificial Intelligence (AI) powered automated Computer-Aided

Detection (CAD) systems. Over the last decade, significant advancements in the computational capabilities of graphical processing units (GPUs), which can perform tera-scale floating-point operations per second [21], along with the vast availability of medical imaging data estimated at 4.2 billion diagnostic examinations conducted globally each year [22], have driven substantial growth in research and development. This progress has focused on integrating AI techniques, including machine learning (ML) and deep learning (DL) models, into a wide range of healthcare applications [23]. A successful example of this is the application of AI in digital breast tomosynthesis, which has reduced radiologist workloads by 40% [24]. Similarly, AI-based cancer detection algorithms have reduced workloads by more than 50% [25]. These examples demonstrate the potential of computer-aided systems to assist radiologists and increase their productivity.

In clinical practice, automated CAD systems must achieve a high level of specificity to minimize the burden on radiologists caused by false positives. At the same time, these systems must also maintain sufficient sensitivity to provide meaningful contributions, such as automatically prioritizing emergency cases for urgent review. With this goal in mind, our focus is on developing a CAD system that leverages advanced image processing and analysis techniques, alongside state-of-the-art deep learning architectures, for the automated analysis of contrast-enhanced chest CT scans. This system is designed to assist in diagnosing pulmonary embolism and other cardiovascular diseases, enhancing both accuracy and efficiency in clinical workflows.

Thesis Outline

This thesis provides an overview of the medical and technological aspects of solutions developed for the automated evaluation of CTPA volume images for CVDs and is structured as follows:

The next section provides essential medical and imaging knowledge to support the understanding of PE and the great vessels within the chest cavity. It begins with an anatomical overview of the thoracic cavity, including the right and left pleural cavities and the mediastinum. The discussion then shifts to the role of medical imaging in diagnosing PE, with a specific emphasis on CTPA. Subsequent sections explore the radiological challenges in imaging and provide a comprehensive background on pulmonary embolism. The third section delves into digital image processing techniques applicable to CTPA imagery, including image acquisition, enhancement, binary morphological processing, segmentation, and feature recognition. The fourth section introduces deep learning methodologies, emphasizing neural networks, convolutional neural networks, the U-Net architecture, and the advanced nnU-Net framework. The fifth section presents the current investigation, outlining its aims, materials,

and findings from three papers, including their background, methods, results, and discussions. Finally, the thesis concludes with insights into the implications of this work and potential future directions.

Medical Context

Thoracic Cavity

The thorax is a major part of the body located in the chest, between the neck and the abdomen. It is enclosed by the thoracic cage, which includes the ribs, sternum, and thoracic vertebrae [26]. The thoracic cavity is divided into three compartments: the right pleural cavity, located on the right side of the chest; the left pleural cavity, located on the left side of the chest; and the mediastinum, which lies between the two pleural cavities. The right pleural cavity contains the pleura, pleural fluid, and the right lung. The right lung primarily consists of the bronchial tree, along with lobar, segmental, and sub-segmental branches of the pulmonary arteries and pulmonary veins.

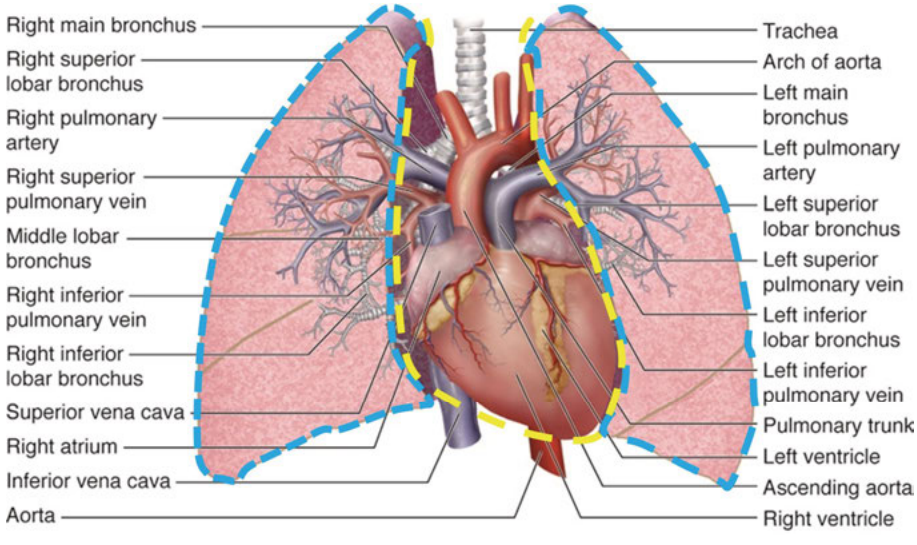

Figure 1. Anatomy of the lungs and heart within the mediastinum and pleural cavities. This illustration details the key anatomical features of the respiratory and cardiovascular systems, highlighting the trachea, main bronchi, lobar bronchi, pulmonary arteries, pulmonary veins, superior vena cava, inferior vena cava, and the chambers of the heart (atria and ventricles). The mediastinum, marked by yellow dashed lines, shows the central thoracic area that contains the heart, major blood vessels, and other structures. The pleural cavities, enclosing the lungs, are outlined with blue dashed lines to emphasize the division of the thoracic cavity into distinct regions. Courtesy of AnatomyTOOL.Org [27].

Similarly, the left pleural cavity houses the pleura, pleural fluid, and the left lung. Like the right lung, the left lung primarily contains the bronchial tree, as well as lobar, segmental, and sub-segmental branches of the pulmonary arteries and pulmonary veins (**Figure 1**) [28].

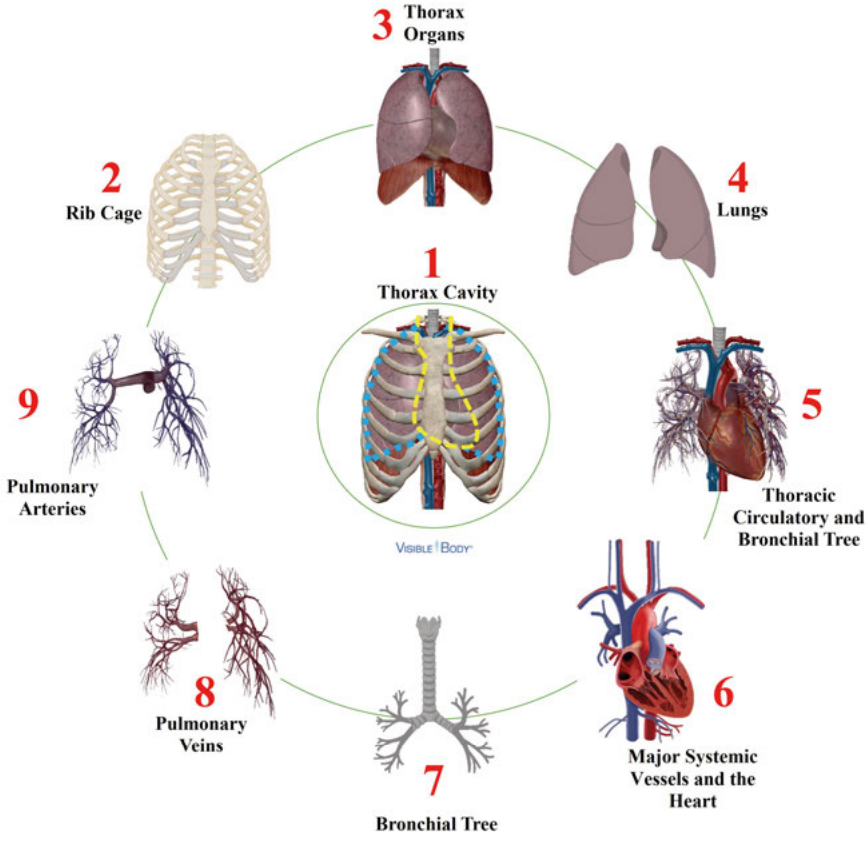

Figure 2. Stepwise visualization of organs and structures in the thoracic Cavity. (1) All thoracic organs shown in 3D, including the rib cage, lungs, and systemic circulatory structures, with the mediastinum depicted in yellow dashed lines and pleural cavities outlined with blue dotted lines. (2) Rib cage isolated for structural reference. (3) Rib cage removed to display lungs and thoracic circulatory anatomy. (4) The right and left lungs were visualized independently. (5) With the lungs removed, the thoracic circulatory system and bronchial tree were clearly visualized (6) Major systemic vessels and the heart displayed in isolation. (7) Bronchial tree shown independently. (8) Pulmonary veins visualized exclusively. (9) Pulmonary arteries visualized exclusively. Images in panels (1), (3), (5), (8), and (9) were created using Human Anatomy Atlas version v2017.1.27, courtesy of Visible Body [29]. Images in panels (2), (4), (6), and (7) were created in https://BioRender.com.

The lungs are essential organs of the respiratory system, responsible for delivering oxygen to the bloodstream and removing excess carbon dioxide from

the body. Pulmonary vessels, including arteries and veins, play a crucial role in blood circulation within the lungs. The pulmonary artery (PA) carries deoxygenated blood from the heart to the lungs, while the pulmonary veins transport oxygenated blood from the lungs back to the heart [30].

The central compartment of the thoracic cavity, known as the mediastinum, is a visceral space located between the left and right pleural cavities. The mediastinum is divided into two main sections: the superior mediastinum and the inferior mediastinum. The inferior mediastinum is further subdivided into three regions: the anterior, middle, and posterior mediastinum. This central compartment of the thoracic cavity contains several vital structures, including the heart, trachea, tracheal bifurcation, and oesophagus. It also contains major blood vessels, such as the pulmonary trunk, the right and left pulmonary arteries and veins, the ascending and descending thoracic aorta, the aortic arch, and the superior vena cava and inferior vena cava, along with other essential organs [31,32]. To enhance the understanding of the anatomy and spatial relationships of these structures, **Figure 2** presents a step-by-step visualization of the thoracic cavity and its major organs. This illustration provides an in-depth, layer-by-layer depiction, aiding in a clearer grasp of the organization and interactions within the thoracic cavity.

Medical Imaging

Medical imaging encompasses a range of specialized methods and techniques used to visualize a patient's internal structures for both diagnostic and therapeutic applications. The origins of this field date back to 1895, with the German physicist Wilhelm Conrad Röntgen's discovery of X-rays [33]. X-rays are a high-energy form of electromagnetic radiation with very short wavelengths. They can penetrate materials like human tissue, which typically absorb or reflect visible light [34]. This penetrating ability makes X-rays valuable in medical imaging for visualizing bones, organs, and other internal structures, helping diagnose conditions such as fractures and tumours.

In contemporary medicine, medical imaging systems are essential and closely linked with radiology, a medical specialty focused on the use of imaging for diagnosis and treatment. Depending on clinical requirements, various imaging modalities are utilized, including X-rays, CT, Magnetic Resonance Imaging (MRI), Ultrasound, and Nuclear Medicine techniques such as Positron Emission Tomography (PET) and Single Photon Emission CT (SPECT) [35].

Computed Tomography

Medical imaging field saw significant advancements in the 1970s with the invention of CT by British engineer Godfrey Newbold Hounsfield based on theoretical calculations by Allan M. Cormack [34]. CT, also known as X-ray

computed tomography or computerized axial tomography (CAT) scan, is an imaging technique that uses rotating X-ray sources and detectors to capture multiple "slice" views of the body from different angles. These two-dimensional (2D) cross-sectional images, derived from three-dimensional (3D) structures, are reconstructed using mathematical algorithms to provide detailed internal views of tissues and organs. CT technology comes in various forms, including Standard (Conventional) CT, Helical (Spiral) CT, High-Resolution CT, Multiple-Row Detector CT, and Dual Source CT. Each variation offers different levels of scanning speed, image quality, and dose efficiency [36]. During the scan, the patient lies on a motorized table that moves through the gantry while the X-ray source rotates around them. Detectors collect the exiting X-rays to generate snapshots, and a computer then compiles these images into precise axial slices [37].

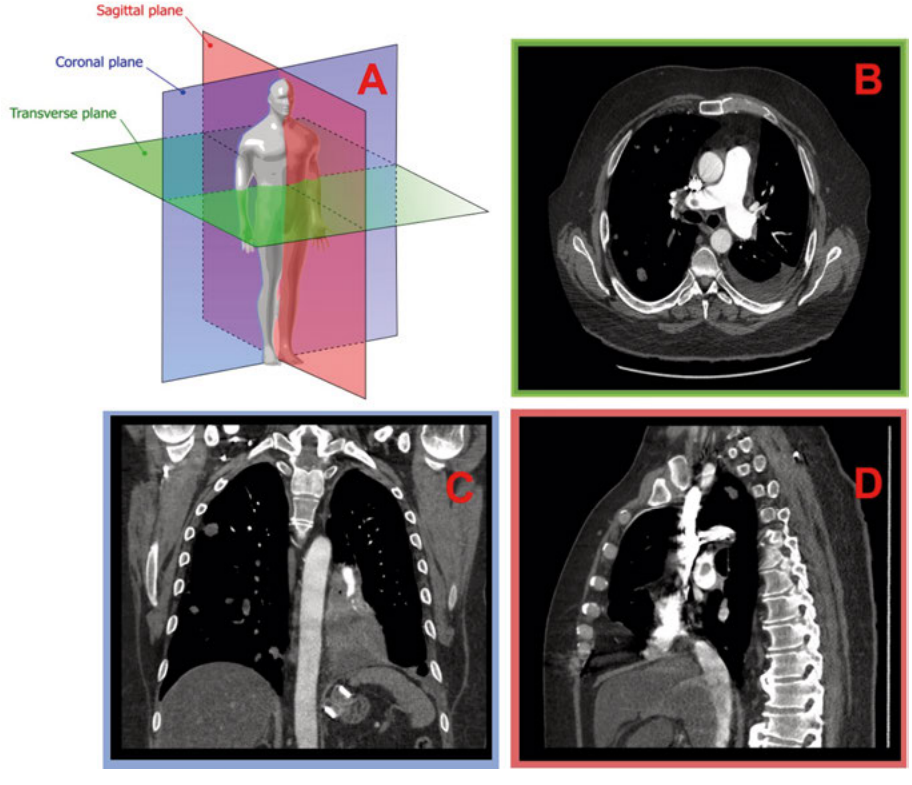

Figure 3. The principal anatomical planes of CTPA volume images. A. The three imaginary anatomical planes on the human body (courtesy of ref. [38]). B. Chest CTPA examination in axial (transverse) (B), coronal (C) and sagittal (D) plane.

Computed Tomography Pulmonary Angiography

CT Pulmonary Angiography (CTPA) is a diagnostic imaging technique that involves injecting an iodine-based contrast agent to increase blood vessel density, thereby improving the visualization of vascular structures in CT scans [39]. Following the injection, a series of X-ray images is captured, providing detailed insights into potential blockages or abnormalities within the pulmonary circulation. The iodine-containing contrast medium (ICCM) enables visualization of the pulmonary arteries from the main level down to the sub-segmental branches [40].

As blood clots do not absorb the contrast agent, they appear as intravascular filling defects within the pulmonary arteries, allowing for their identification [41,42]. A CTPA examination contains a sequence of 2D cross-sectional CT images which together form a 3D volume image. 2D cross-sectional CT images can be visualized in three principal anatomical planes axial, coronal, and sagittal (**Figure 3**).

Pulmonary Embolism

Venous thromboembolism (VTE) refers to a blood clot that forms in a vein and encompasses pulmonary embolism (PE) and deep vein thrombosis (DVT) [43]. Pulmonary embolism occurs when a clot from a DVT travels to the lungs [44,45], making it a common and potentially fatal complication of VTE [46]. Following myocardial infarction and stroke, PE ranks as the third most common cause of death from cardiovascular disease [47] and is the leading cause of preventable deaths in hospitals worldwide [48]. Each year, PE affects over 400,000 individuals in Europe [49] and between 300,000 and 600,000 people in the United States [50], resulting in an estimated 100,000 or more deaths [51].

The risk of developing a PE can be classified as unprovoked (also known as idiopathic or primary) or provoked (also known as secondary). Unprovoked risk factors include being over 65 years of age, obesity, smoking, hypertension, prolonged travel (particularly in a seated position), and thrombophilia. In contrast, provoked risk factors encompass recent surgery or trauma, prolonged immobility (including during the postoperative period), cancer, pregnancy, pneumonia, and congestive heart failure [44,52].

The clinical signs and symptoms of PE typically include shortness of breath (dyspnoea) and chest pain, often described as sharp, stabbing sensations that worsen with deep breathing or coughing. Patients frequently exhibit an increased heart rate (tachycardia, >100 beats per minute) and a rapid respiratory rate (tachypnoea, >20 breaths per minute) as the body attempts to compensate for decreased oxygen levels and impaired circulation. Additional

common symptoms include coughing, which may be dry or accompanied by blood-streaked sputum (haemoptysis) [53].

Diagnosis of Pulmonary Embolism

Diagnosing PE typically involves a well-structured approach that relies on non-invasive techniques, allowing clinicians to confirm (rule in) or exclude (rule out) PE while minimizing unnecessary testing [44]. Various clinical models have been developed to guide the diagnosis of PE [17,43,52]. The general outline of a commonly used diagnostic algorithm is summarized below.

The first step is to estimate the likelihood of PE, which can be done either through clinical judgment or by using validated scoring systems such as the Wells Score [54] or the revised Geneva Score [55]. These tools incorporate factors like signs of deep vein thrombosis, recent surgery or immobilization, active cancer, and haemoptysis to assess the probability of PE [56].

When these scores categorize a patient as low risk, the Pulmonary Embolism Rule-out Criteria (PERC) may be applied to refine the likelihood even further. PERC consists of eight clinical parameters, such as age under 50, heart rate under 100 beats per minute, adequate oxygen saturation, and absence of unilateral leg swelling. If a low-risk patient satisfies all PERC criteria (i.e., is "PERC negative"), additional testing for PE is generally unnecessary. However, if a patient does not meet PERC requirements, or if the clinical suspicion based on Wells or Geneva remains moderate or high, the next step is to measure D-dimer levels. A normal D-dimer in an appropriately selected patient can rule out PE, whereas an elevated D-dimer calls for imaging [52,57].

The current gold standard for diagnosing suspected PE is CTPA, which allows direct visualization of the pulmonary vasculature to detect any clots [17,58]. At the level of the carina of trachea, the main pulmonary arteries (also known as the pulmonary trunk) bifurcate into the right and left main PA. The right and left PA subsequently split into lobar, segmental, and subsegmental branches (52). PE can occur at each of these PA levels (**Figure 4**). In general, there is high concordance between radiologists in diagnosis of PE up to the segmental level, but lower concordance on subsegmental emboli (20,53).

In summary, by integrating clinical probability assessment, applying the PERC rule to selected low-risk patients, conducting targeted D-dimer testing, and confirming findings with CTPA, clinicians can accurately confirm or rule out pulmonary embolism in a stepwise manner.

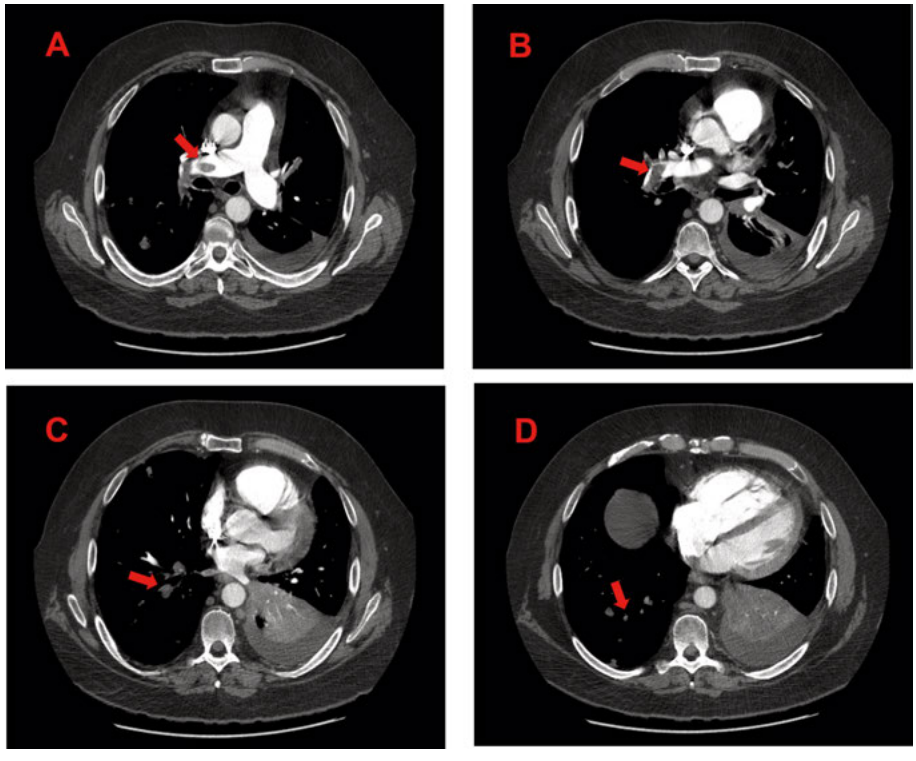

Figure 4. The appearance of PE in different levels of the pulmonary arteries in CTPA volume images. The red arrow shows PE at the main (A), the right lobar (B), the segmental (C) and subsegmental (D) pulmonary artery levels. The CT images were acquired in the axial plane at slice thickness of 2.0 mm, WL: 100 HU, WW: 600 HU.

Radiological Challenges

Due to various physical, technical, and patient-related factors, distortions and unwanted effects, collectively known as CT artifacts, can appear in CT images. CT image artifacts can be classified based on their appearance into four major categories: streaking, rings and bands, shading, and miscellaneous artifacts [59]. However, when classified by their primary cause, these artifacts fall into four categories: physics-based artifacts (such as beam hardening and noise), patient-based artifacts (including motion and breathing artifacts, as well as metal artifacts), scanner-based artifacts (like ring artifacts from detector malfunctions), and artifacts from helical and multisection techniques [60]. **Figure 5** illustrates several common artifacts observed in our study cohort (refer to the Materials section), accompanied by sample images demonstrating their appearance on CTPA scans.

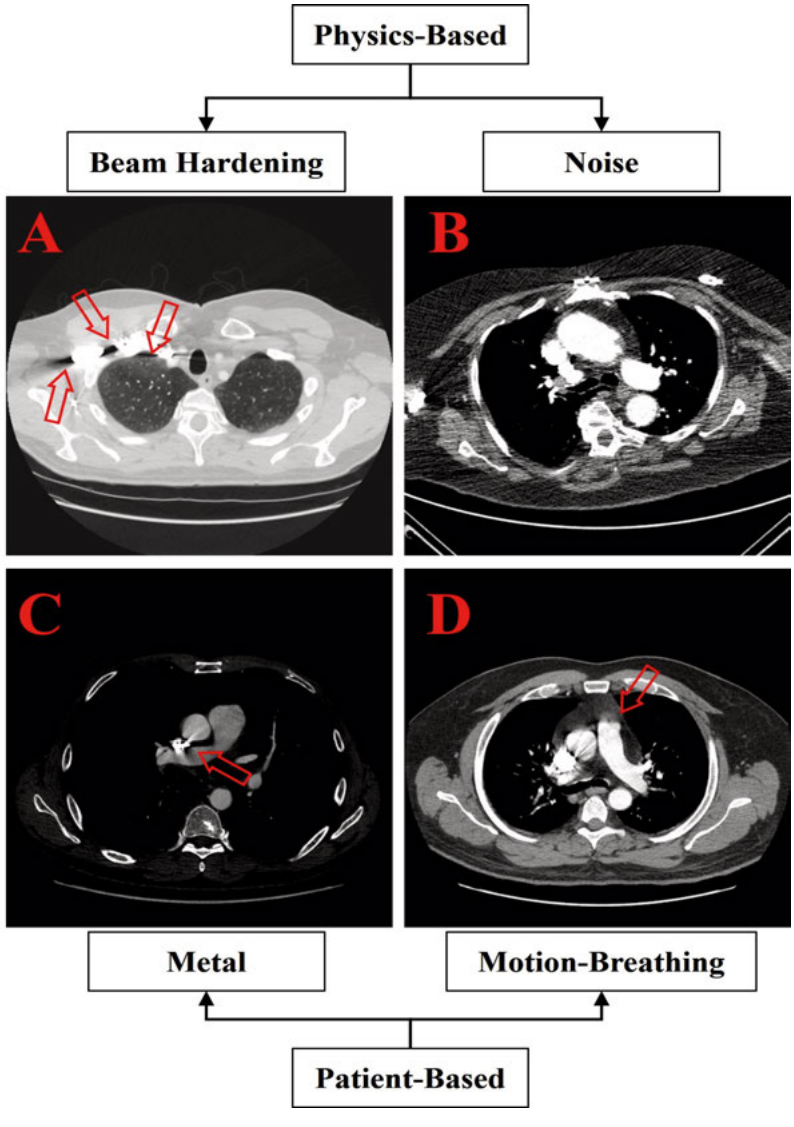

Figure 5. Most frequent image artifacts in the internal dataset. Panel A shows beam hardening artifacts indicated by the arrow (WL: -400 HU; WW: 1500 HU). In Panel B, noise is observed throughout the image (WL: 40 HU; WW: 400). Panel C displays artifacts caused by a metallic object in the superior vena cava, indicated by the arrow (WL: 300 HU; WW: 600). Panel D illustrates a motion artifact resulting in a blurry and double image of the pulmonary trunk (WL: 40 HU; WW: 400).

Digital Image Processing and Analysis Techniques Applicable to CTPA Imagery

Digital image processing and analysis involve extracting information from digital images [61] and are a subfield of digital signal processing. A digital image can be represented as a two-dimensional signal, formulated mathematically as a function of two independent variables, for example, $f(m,n) = g$. By introducing an additional independent variable, such as $f(m,n,z) = g$, three-dimensional (3D) volume images can be generated. Here, m, n, and z represent the coordinates of the smallest unit of the image. In two-dimensional (2D) images, this smallest unit is referred to as a pixel, while in 3D images, it is called a voxel. For CT pulmonary angiography (CTPA) volume images, m and n are the independent variables that define the image matrix, determined by the spatial resolution capacity of CT scanners. At present, a matrix size of 512×512 is the standard for most CT scanners [62]. The independent variable z corresponds to the total number of individual images (slices) in the CTPA volume. The slice thickness, a parameter of CT image acquisition, determines the value of z. Together, these variables define the CTPA volume images, which can be visualized as shown in **Figure 6**.

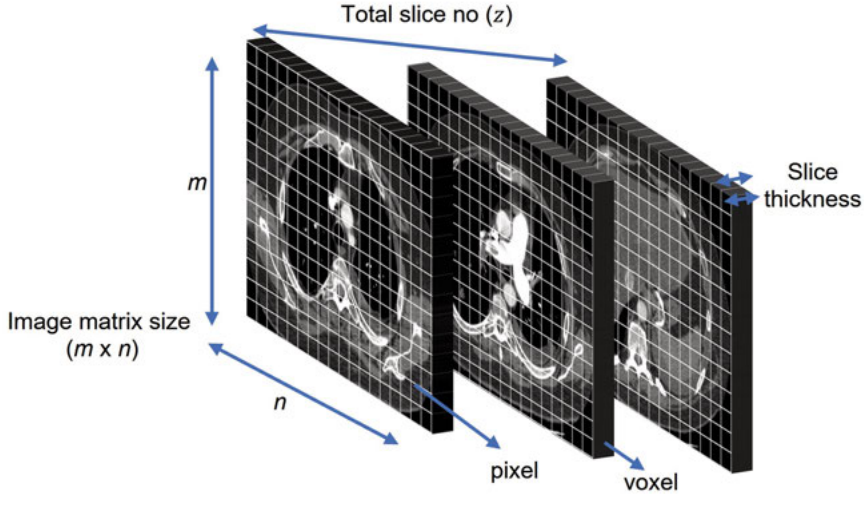

Figure 6. An illustration of CTPA volume images with fundamental definitions. The white grids on the slices are imaginary lines used to indicate pixels and voxels.

Furthermore, g represents the intensity of the image at a specific location, determined by m, n, and z. In CTPA volume images, g corresponds to radiodensity, which is measured using the Hounsfield Unit (HU) scale. The HU scale is a linear transformation of the linear attenuation coefficient of water at room temperature [63]. **Table 1** provides the HU scale values for various materials commonly observed in CTPA imaging [64,65].

Table 1. Hounsfield unit values for different tissues in CTPA examinations.

Materials	HU
Air	-1000
Lung	-900 to -200
Fat	-100 to -20
Water	0
Blood	20 to 90
Muscle	40 to 60
Spongy Bone	30 to 230
Compact Bone	>250
Foreign body	>1000

Note. — CTPA volume images have a HU range of 4096, from -1000 HU (air) to +3000 HU (metallic object), with shades of gray per pixel.

An image analysis problem can be addressed through several fundamental steps, each comprising a range of algorithms and methods [66]. In the following sections, we focus on five key steps: image acquisition, image enhancement, binary morphological image processing, segmentation, and feature recognition and classification, along with their associated methodologies. Nevertheless, the most crucial technique in digital image processing, which we must address first, is convolution.

Convolution

Convolution is a mathematical technique used to merge two functions, resulting in a third function. This technique involves shifting one function across the other, calculating the product of their overlapping values at each step, and summing these results to produce the final outcome [67]. It is a crucial operation widely utilized in image processing applications such as sharpening, blurring, enhancing images, detecting edges, and extracting features.

In image processing, the first function is referred to as the input image, while the second function is known as the filter or kernel. The convolution operation can be mathematically represented as:

$$\boldsymbol{O(i,j)} = \sum_{\boldsymbol{m=-f}}^{\boldsymbol{f}} \sum_{\boldsymbol{n=-f}}^{\boldsymbol{f}} \boldsymbol{F(m,n)} \cdot \boldsymbol{I(i+m, j+n)} \quad \textbf{(1)}$$

Where:

$\boldsymbol{f}$ represents half the size of the filter, $\boldsymbol{O(i,j)}$, is the output pixel value at position $\boldsymbol{(i,j)}$, $\boldsymbol{F(m,n)}$ is the filter value at position $\boldsymbol{(m,n)}$, and $\boldsymbol{I(i+m, j+n)}$, is the corresponding pixel in the image.

Image Acquisition

Retrieving an image from its source is the first step in any digital image processing and analysis problem. The internal CTPA dataset used in this thesis was obtained from the Picture Archiving and Communication System (PACS, Sectra AB, Linköping, Sweden) in Digital Imaging and Communications in Medicine (DICOM) format. DICOM is an internationally recognized standard commonly used for storing and transferring data in medical imaging. A DICOM file contains raw image data along with metadata related to CT image acquisition procedures and patient information [68,69].

Image Enhancement

Image enhancement is the process of improving the quality of digital images to facilitate further processing and analysis [70]. In this study, we employed Gaussian smoothing methods to reduce noise and suppress unnecessary details in CTPA volume images. Gaussian smoothing is highly effective for noise reduction and computationally efficient. Applying the Gaussian smoothing method to a digital image involves convolving the image with a Gaussian filter kernel. The Gaussian filter kernel is generated using the Gaussian function:

$$\boldsymbol{G(m,n)} = \frac{\boldsymbol{1}}{\boldsymbol{2\pi\sigma^2}} \boldsymbol{e}^{-\frac{\boldsymbol{m^2+n^2}}{\boldsymbol{2\sigma^2}}} \quad \textbf{(2)}$$

Here, $\boldsymbol{\sigma}$ represents the standard deviation of the Gaussian distribution. The Gaussian smoothing method reduces image noise while also diminishing image details. However, in certain situations, preserving image details, such as

object edges, is essential (**Figure 7**). Anisotropic diffusion, also known as Perona-Malik diffusion, addresses this by reducing noise while maintaining important details in the image [71]. The anisotropic diffusion method can be expressed as:

$$\boldsymbol{I_t = div(c(m,n,t)\nabla I) = c(m,n,t)\Delta I + \nabla c \cdot \nabla I} \quad \textbf{(3)}$$

Here, I represents the image, t is the iteration variable, and $\boldsymbol{\nabla}$, **div**, and Δ denote the gradient, divergence, and Laplacian operators, respectively. The diffusion coefficient function, $\boldsymbol{c(m,n,t)}$, can be expressed as:

$$\boldsymbol{c(||\nabla I||) = e^{-(||\nabla I||/K)^2}} \quad \textbf{(4)}$$

Here, $\boldsymbol{K}$ is a constant that determines the sensitivity to edges.

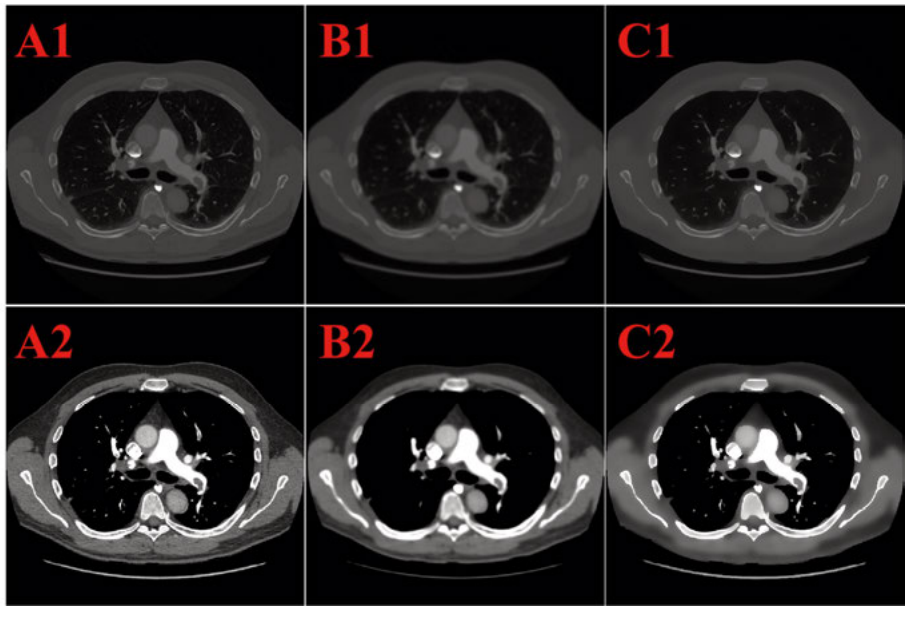

Figure 7. Example of Gaussian smoothing and anisotropic diffusion operations. To better understand the applied operations, two different values of window level (WL) and window width (WW) are provided. In the first row (A1, B1, and C1), WW is set to 4094 HU and WL to 1023 HU; in the second row (A2, B2, and C2), WW is set to 600 HU and WL to 100 HU. The original image is shown in A1 and A2. The result of the Gaussian smoothing operation, with a sigma ($\boldsymbol{\sigma}$) value of 2, is shown in B1 and B2. The result of the anisotropic diffusion operation is shown in C1 and C2. As can be seen above, in Gaussian smoothing operations, image details are blurred, whereas in anisotropic diffusion operations, the details are preserved.

Binary Morphological Image Processing

Binary morphological image processing is a technique used to manipulate binary images using a small, pre-defined binary shape, known as the structuring element (SE), which is essentially a matrix of pixels. Applying morphological operations to a digital image involves convolving the image with the SE. The purpose of morphological image processing is to evaluate whether the SE fits, hits, or misses an object within the binary image. In this study, we utilized four fundamental morphological operations for binary object manipulation: erosion, dilation, opening, and closing. The opening and closing operations are derived from the basic operations of erosion and dilation [72]. An example of binary morphology operations is given in **Figure 8**.

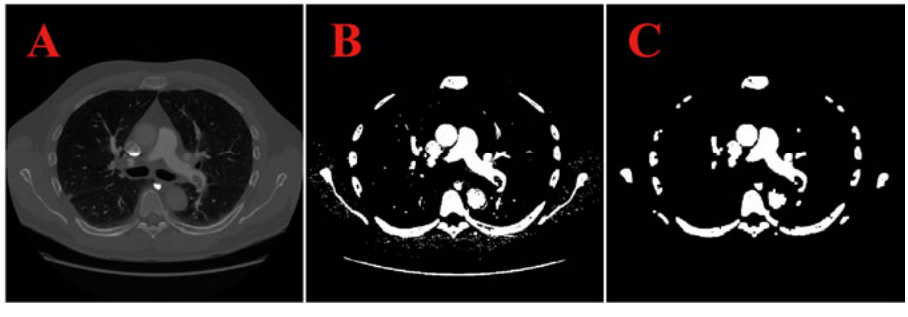

Figure 8. Example of a binary morphological operation. The original image (A) is first thresholded with a 100 HU cut-off value, as shown in B. Then, the opening operation with a disk-shaped structuring element and a matrix size of 3 pixels is applied to the thresholded image. The result is shown in C.

Segmentation

Segmentation is the process of dividing an image into regions of interest (ROI) that share similar characteristics, such as intensity, texture, pattern, or location [73]. It is the most critical step in image analysis, as all subsequent calculations and measurements rely on accurately defined ROI [66]. However, segmentation is also the most challenging step in the process. Detecting pulmonary embolism (PE) in CTPA volume images represents a segmentation problem. The ROI to be segmented is the pulmonary artery (PA) because PE occurs exclusively within the PA system. However, the PA is a complex anatomical structure that is difficult to segment accurately. The segmentation methods employed in this thesis are described in the following section.

Thresholding

A threshold value is defined, and pixels or voxels are classified as background or foreground based on whether their intensity values fall below or above this cut-off value. Thresholding is the simplest segmentation method and can be expressed as:

$$f(m,n) = \begin{cases} 0, & if\ g(m,n) \leq T \\ 1, & if\ g(m,n) > T \end{cases} \quad \textbf{(5)}$$

Here, $f(m,n)$ represents the binary output image, $g(m,n)$ is the grayscale input image, and T is the threshold value. **Figure 8-B** illustrates an example of a basic thresholding operation.

Region Growing

This region-based image segmentation method begins with the selection of seed points (pixels or voxels). A region-growing criterion is then applied to identify and include adjacent pixels or voxels that meet the specified condition. This method is computationally efficient and performs well when accurate seed points are selected [74]. However, the primary challenge lies in the selection of these seed points. If the process is not automated with high accuracy, it can significantly increase the user's workload.

The region-growing method can be applied to both 2D and 3D binary or grayscale images. The sensitivity of the algorithm in defining regions depends on the connectivity parameters. For an $(m \times n)$ image matrix, either 4-pixel or 8-pixel connectivity can be used. For an $(m \times n \times z)$ volume matrix, connectivity options include 6, 18, or 26 voxels. A higher connectivity value enables the algorithm to segment regions faster and cover more area or volume.

Edge Detection

Edge detection is a technique used to identify the boundaries of objects by detecting sudden changes in intensity within an image. This is typically achieved by convolving the image with specialized edge detection operators (filters). Commonly used edge detection operators include the Laplacian, Prewitt, Sobel, and Canny operators [66]. The combination of the Canny operator and the Hessian matrix provides an effective vesselness filter, making it particularly useful for detecting vascular structures. Therefore, in this study, we utilized the Canny operator and the Hessian matrix for edge detection (**Figure 9**). The Hessian matrix is defined as:

$$\boldsymbol{H_{mn}} = \begin{bmatrix} \boldsymbol{I_{mm}(v)} & \boldsymbol{I_{mn}(v)} \\ \boldsymbol{I_{mn}(v)} & \boldsymbol{I_{nn}(v)} \end{bmatrix} \quad \textbf{(6)}$$

Here, v represents a voxel in the image, $\boldsymbol{I_{mm}}$ is the second derivative of the image in the horizontal direction, $\boldsymbol{I_{nn}}$ is the second derivative in the vertical direction, and $\boldsymbol{I_{mn}}$ is the partial derivative of the image in both horizontal and vertical directions. The eigenvalues of the Hessian matrix provide critical information about the structure of an object. Consider the eigenvalues $\boldsymbol{\lambda_1}$ and $\boldsymbol{\lambda_2}$ of $\boldsymbol{H_{mn}}$:

- If both $\boldsymbol{\lambda_1}$ and $\boldsymbol{\lambda_2}$ are large, it indicates a corner
- If one of $\boldsymbol{\lambda_1}$ and $\boldsymbol{\lambda_2}$ is large and the other small, it indicates a step edge
- If both $\boldsymbol{\lambda_1}$ and $\boldsymbol{\lambda_2}$ are small, it indicates a low-contrast region

Figure 9. Example of edge detection operations. The original image is shown in panel A. The Canny edge detection operation is applied, as shown in panel B. The eigenvalue of the Hessian matrix is calculated on the original image, and the result is displayed in panel C.

Feature Recognition and Classification

The final step in digital image processing and analysis is feature recognition and classification. Feature recognition involves detecting or identifying objects within an image, while classification entails grouping these detected objects into predefined categories or classes. Object detection and classification can be achieved using statistical methods or structural methods. Statistical methods, such as those based on deep learning, will be discussed in the next section. Here, we provide a brief overview of a basic object detection method.

Connected Component Labelling

Connected Component Labelling (CCL) is an object detection method used to identify connected regions in binary images [75]. CCL can be applied to 2D or 3D binary or grayscale images. For an $(m \times n)$ image matrix, either 4-pixel or 8-pixel connectivity can be used. For an $(m \times n \times z)$ volume matrix, connectivity options include 6, 18, or 26 voxels. The CCL algorithm for binary images can be summarized in three basic steps:

1. The input image is converted into a binary image.
2. Voxels are grouped based on the specified voxel connectivity parameter.
3. The grouped voxels are labelled sequentially according to their group order and count (**Figure 10**).

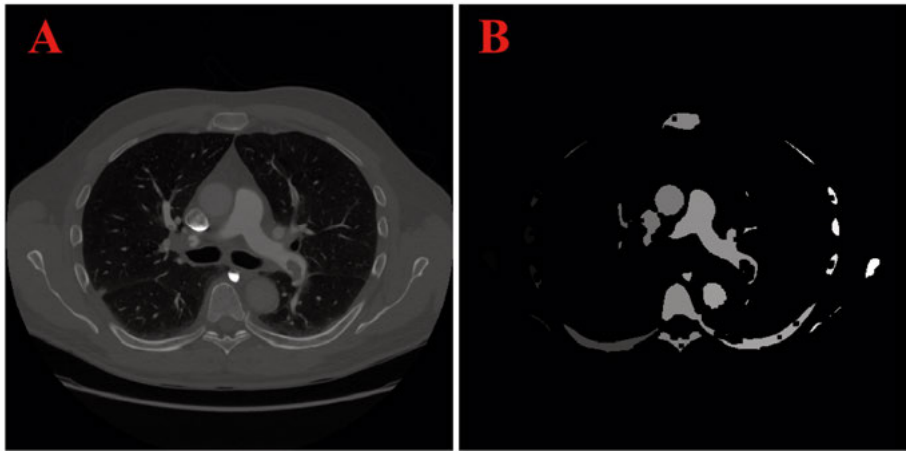

Figure 10. Example of connected component labelling operations. The original image is shown in panel A. First, an anisotropic diffusion operation was applied to the original image to enhance it. Next, an erosion morphological operation was applied. Then, the image was thresholded at 100 HU to capture potential blood vessels. Finally, a connected component labelling algorithm was applied to detect and separate each component. As shown in panel B, each component is represented with different grayscale values.

Deep Learning

Artificial intelligence (AI), at its core, involves enabling machines to perform tasks typically associated with human intelligence. Machine learning (ML), a subset of AI, allows machines to acquire skills and learn from experience without direct human intervention [76]. Deep learning (DL), a further subset of ML, leverages artificial neural networks (ANNs) to progressively extract higher-level features from input data [77]. ANNs are computational algorithms inspired by biological neural networks, while deep neural networks (DNNs) are ANNs with multiple layers that enable more complex processing.

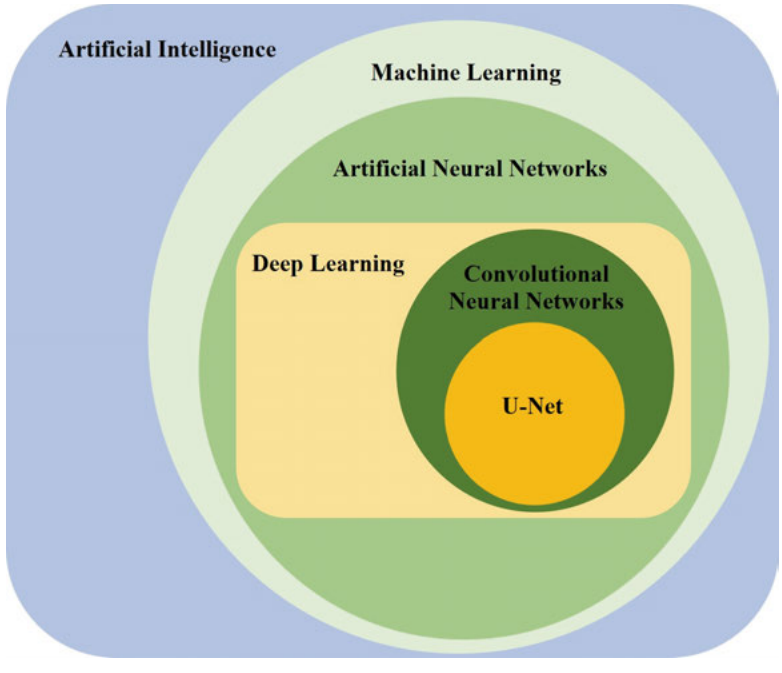

Figure 11. Hierarchical relationship in Artificial Intelligence (AI). Machine Learning (ML) as a subset of AI, Artificial Neural Networks (ANNs) as a subset of ML, Deep Learning (DL) within ANNs, Convolutional Neural Networks (CNNs) as a specialization of DL, and U-Net as a specific architecture within CNNs.

Within ANNs, convolutional neural networks (CNNs) form a specialized subset. CNNs comprise at least one convolutional layer, a pooling layer, and a non-linear activation function. Each layer performs specific mathematical

operations and can be understood as a mathematical function. Among deep learning architectures, deep convolutional neural networks (DCNNs) are particularly well-suited for semantic segmentation tasks [78]. Given that our problem involves semantic segmentation, we focused on the U-net architecture, a specific and widely recognized DCNN model designed for this purpose [79]. Meanwhile, **Table 2** summarizes other architectures recommended for various tasks. These concepts are presented in a hierarchical structure in the form of a Venn diagram as shown in **Figure 11**, and they are broadly defined in the following sections.

Table 2. Comprehensive overview of various architectures and their use cases in computer vision tasks.

Architectures	Use Cases
LeNet [80,81]	Handwritten digit recognition
AlexNet [82]	Large-scale image classification
VGGNet [83,84]	Image classification and object detection
GoogleNet [85,86]	Image classification and feature extraction
ResNet [87,88]	Image recognition and object detection
DenseNet [89]	Image classification
EfficientNet[90,91]	Image classification and object detection
MobileNet [92,93]	Mobile and embedded vision applications
YOLO [94–96]	Object detection and real-time video analysis
R-CNN [97,98]	Object detection and instance segmentation
Capsule Networks [99,100]	Image classification and object detection
Generative Adversarial Networks [101–103]	Image synthesis
Atrous Convolutions [104,105]	Semantic segmentation
SqueezeNet [106]	Image classification
ShuffleNet [107,108]	Mobile and embedded vision applications
NASNet [109]	Image classification and recognition
Vision Transformers [110,111]	Classification, detection and segmentation
Recurrent CNNs [112,113]	Object recognition, time-series analysis
Octave Convolution Networks [114]	Image and video recognition
Spatial Transformer Networks [115]	Image classification and object detection
Foundation Models [116,117]	Image classification and object detection
Fully Convolutional Networks [118,119]	Semantic segmentation
Big Transfer [120]	Image classification

Note. — CNNs: convolutional neural networks, R-CNN: Region based CNNs.

Artificial Neural Networks

Artificial Neural Networks (ANNs) take inspiration from the architecture and functionality of biological neurons. In the human brain, neurons gather signals through dendrites, process them within the soma, and transmit an output signal via the axon when a certain threshold is surpassed. Similarly, an artificial neuron combines weighted input signals and uses a non-linear activation function to generate its output [121] (**Figure 12**).

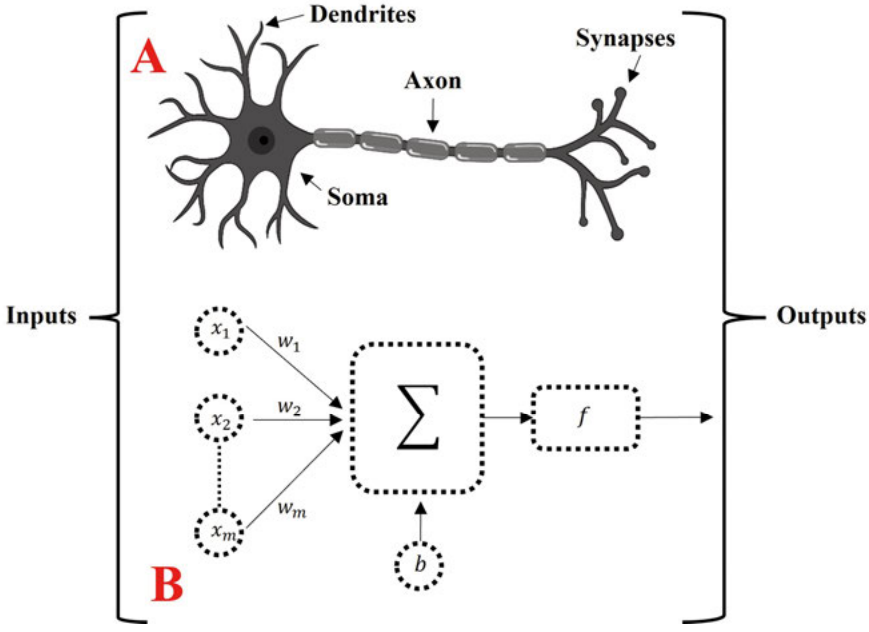

Figure 12. Schematic illustrations of both biological and artificial neurons are presented. Panel A shows a biological neuron (created in https://BioRender.com), while Panel B illustrates an artificial neuron (AN). In an AN, the inputs ($x_{i\ to\ m}$) serve the same purpose as dendrites, namely receiving information. The weights ($w_{i\ to\ m}$) and bias (b) mirror synapse strength and baseline excitability, and the soma (cell body) is represented by the summation ($\sum$) and activation function (f). Finally, the output of the AN corresponds to the signal transmitted along the axon in a biological neuron.

This process can be mathematically described as:

$$\boldsymbol{y = f\left(\sum_{i=1}^{M} w_i x_i + b\right)} \tag{7}$$

Where, x_i represents the inputs, w_i denotes the trainable weights, b is the bias term, and $f(\cdot)$ symbolizes the activation function. By arranging these neurons

into layers and interconnecting them, ANNs are capable of learning intricate mappings from input data to desired outputs [121].

Convolutional Neural Networks

Convolutional Neural Networks (CNNs) are a special type of neural network that use convolution operations (refer to the Digital Image Processing and Analysis Techniques section) instead of traditional matrix multiplications in at least one layer [122]. By focusing on local spatial relationships in grid-like data, such as images or signals, CNNs excel at identifying important features for tasks like image recognition and computer vision [123]. A typical CNN architecture alternates between convolutional layers and pooling layers (**Figure 13**). Pooling (like max pooling or average pooling) reduces the size of the feature maps while keeping essential information.

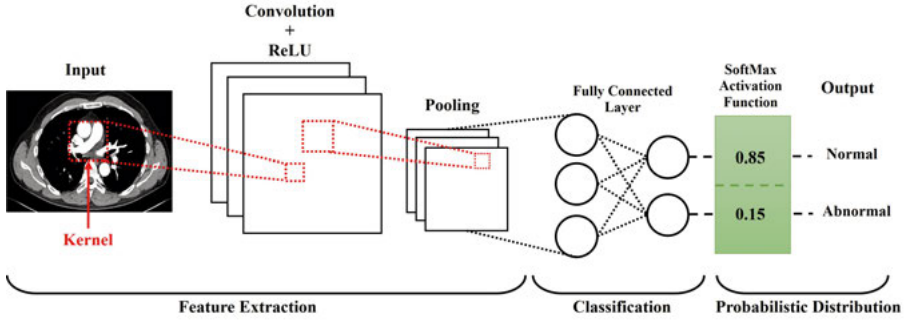

Figure 13. A schematic depiction of a Convolutional Neural Network. A basic CNN architecture can be constructed with a single convolutional layer followed by a single pooling layer and concluded with one fully connected layer.

Activation functions, such as ReLU (Rectified Linear Unit), add non-linearity to help the network learn complex patterns. Towards the end of the network, fully connected (dense) layers combine the features for final classification or regression tasks. Another useful technique is pointwise (1×1) convolution, which helps reduce the size and efficiently combine features across channels. CNNs can have dozens or even hundreds of layers, with each layer refining the features found by previous layers. Through forward propagation and back-propagation, the network's parameters (weights and biases) are adjusted, allowing CNNs to adapt and improve in recognizing the most relevant features for a given task [124].

U-Net

U-Net is a CNN architecture originally introduced by Ronneberger et. al., specifically for biomedical image segmentation [125]. Its success, however, extends well beyond medical imaging [79,126,127] to various segmentation tasks [128,129]. The network's distinctive U-shaped layout arises from two main pathways: a contracting (encoder) path that captures semantic context and an expanding (decoder) path that recovers spatial precision. This design, often referred to as "fully convolutional," was inspired by earlier fully convolutional networks (FCNs) introduced by Long et al. [118], yet U-Net distinguishes itself with extensive use of skip connections. These connections concatenate the feature maps from the encoder to the corresponding layers in the decoder, ensuring that high-level context is effectively combined with spatial details.

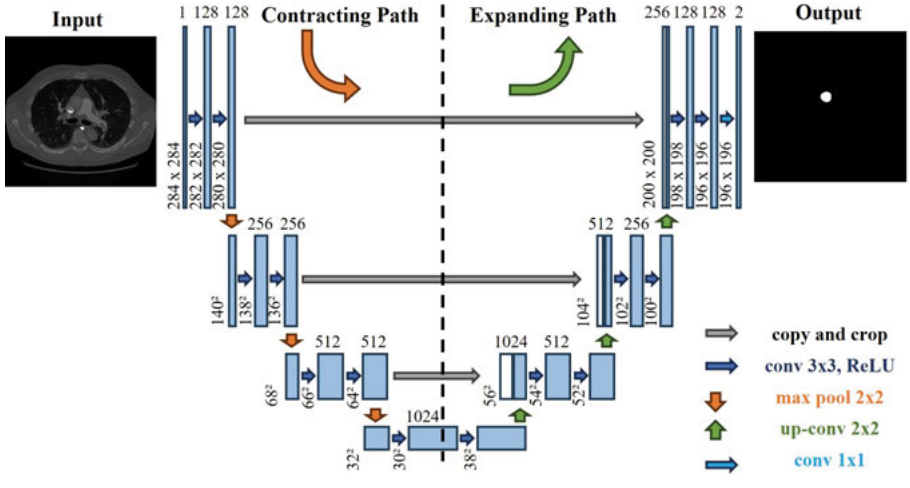

Figure 14. 2D U-net architecture. The figure illustrates the 2D U-Net, comprising a contracting path (left) and an expanding path (right). Blue arrows indicate 3×3 convolutions with ReLU activation, orange arrows denote 2×2 max-pooling layers, and green arrows represent 2×2 up-convolutions. Gray arrows show skip connections that merge features from the contracting to the expanding path. The input is a CT scan slice, and the output is a segmentation mask. Dimensions and feature channels are annotated, showcasing the model's symmetry and ability to retain spatial details for accurate segmentation.

In the contracting path, U-Net employs repeated blocks of 3×3 convolutions, each followed by a ReLU activation, and then a max-pooling operation to progressively reduce spatial dimensions while increasing the number of feature channels. This strategy broadens the receptive field and extracts robust, high-level representations. The bottleneck, which bridges the encoder and decoder, is the network's deepest layer where two 3×3 convolutions and ReLU activations capture abstract semantic features. While this deeper representation is

powerful for classification, it tends to lose spatial localization. To counterbalance this, U-Net's decoder path systematically upsamples the feature maps using transposed convolutions (or up-convolutions). After each upsample, the network concatenates the feature maps from the corresponding encoder level, providing rich localization cues that help reconstruct fine-grained spatial information in the output segmentation map. Finally, a 1×1 convolution layer reduces the number of feature channels to match the target classes, producing a dense prediction for each pixel [126]. **Figure 14** demonstrates how the input image is progressively contracted and then expanded, utilizing skip connections to combine low- and high-level features for accurate segmentation.

A key advantage of U-Net is its ability to produce pixel-level classifications efficiently. By discarding fully connected layers and relying solely on convolutional operations, the architecture can handle images of varying sizes. To further tackle large images, U-Net employs a tiling (or overlap-tile) strategy, mirroring the border regions so that the network retains context near the edges. This allows segmentation of high-resolution images without being constrained by GPU memory limits [125]. Overall, U-Net's flexibility in input handling, its effective skip connections, and its balanced encoder-decoder design have solidified its position as a cornerstone in semantic segmentation tasks, enabling precise object localization alongside a broad contextual understanding for accurate predictions.

nnU-Net

The no-new-U-Net (nnU-Net) is an open-source, self-configuring method designed for deep learning-based biomedical image segmentation [130]. Built upon the widely used U-Net semantic segmentation architecture [125], it provides an automated and standardized pipeline for tasks such as preprocessing, data augmentation, network architecture design, training, postprocessing, and inference. nnU-Net organizes hyperparameters into three categories: rule-based, fixed, and experimental, and its proven success across diverse datasets makes it a transformative tool in medical image segmentation.

Key features include automatic configuration, advanced network architecture, and efficient training and inference. It adapts preprocessing, network design, and postprocessing to dataset-specific properties using rule-based and empirical parameters. The architecture supports 2D U-Net, 3D U-Net (Full Resolution), and 3D U-Net Cascade, employing an encoder-decoder design with skip connections for improved gradient flow (**Figure 15**). Instance normalization ensures stability with small batches, and Leaky ReLU enhances gradient propagation. Training incorporates robust data augmentation techniques such as rotation, scaling, Gaussian noise, and low-resolution simulation. Inference uses a sliding window approach with Gaussian weighting to minimize stitching artifacts, and optimization relies on a combination of cross-entropy and Dice loss functions [130].

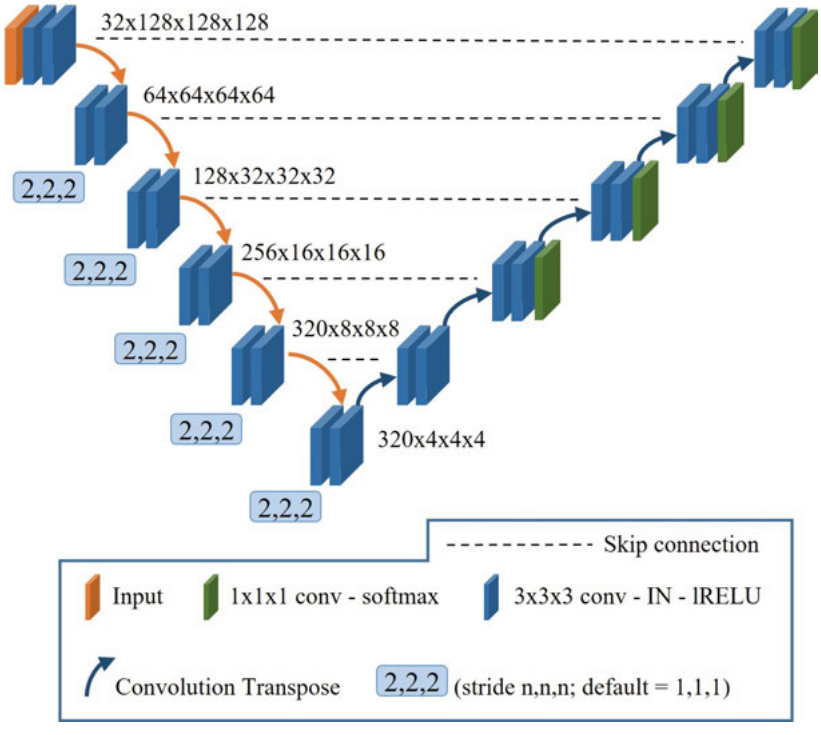

Figure 15. Schematic architecture of the 3D U-Net model generated by nnU-Net. The model consists of a multi-scale encoder-decoder structure with symmetric skip connections. The encoder (left) progressively reduces the spatial resolution of the input while increasing feature dimensionality, starting from 32×128×128×128 and ending at 320×4×4×4. Each encoder block employs 3×3×3 convolution layers with instance normalization (IN) and IReLU activation, followed by down-sampling with stride 2×2×2. The bottleneck layer represents the most compressed representation of the input features. The decoder (right) reconstructs the spatial resolution through transposed convolution layers (stride 2×2×2) and combines features from corresponding encoder levels using skip connections. The output layer uses a 1×1×1 convolution followed by softmax to generate the final segmentation map.

The workflow leverages dataset fingerprinting to extract properties like dimensions, spacing, modalities, and class distribution, while pipeline fingerprinting configures parameters such as patch size and network topology. Empirical selection fine-tunes configurations, choosing between 2D, 3D full resolution, or 3D cascade models and applying connected-component-based postprocessing for refinement. nnU-Net's out-of-the-box usability achieves state-of-the-art results validated by international competitions. It is highly versatile, handling 2D and 3D images across diverse modalities and scales, robust to class imbalances, and capable of managing large datasets [131]. As a standardized benchmark tool, it ensures reproducibility and fair comparisons.

While version 1 of nnU-Net required both raw and ground truth datasets to be in the NIfTI format, version 2 overcomes this limitation by supporting multiple input file types, including PNG, BMP, TIFF, NRRD, MHA, and others.

Widely used in medical imaging, nnU-Net system excels in segmenting structures such as brain tumours [132], liver [133], lungs [134], and cardiac regions [135]. It serves both domain scientists seeking straightforward solutions and AI researchers developing new methodologies [136].

The Present Investigation

Overall Aims

The primary objective of this thesis was to develop and validate automated and deep learning-based algorithms for detecting, segmenting, measuring, and classifying mediastinal structures and vascular features in computed tomography pulmonary angiography (CTPA) examinations, with a particular focus on pulmonary embolism (PE) detection. The aim was to enhance diagnostic accuracy, speed, and efficiency in clinical practice. The specific aims of each paper are outlined below:

Paper I

Automated detection, segmentation and measurement of major vessels and the trachea in CT pulmonary angiography.

To develop a deterministic, fully automated algorithm for detecting, segmenting, and measuring mediastinal structures in CTPA, achieving high accuracy across internal and external datasets while addressing common artifacts and medical conditions.

Paper II

Segmentation and Measurements of Major Vessels from CT Pulmonary Angiography Using Deep Learning.

To develop a deep learning-based approach for the segmentation and measurement of major blood vessels in CTPA, utilizing nnU-Net for segmentation and a deterministic algorithm for measurement, aiming to achieve high correlation with radiologist assessments and robust performance on internal and external datasets.

Paper III

Enhanced Classification Performance using Deep Learning Based Segmentation for Pulmonary Embolism Detection in CT Angiography.

To develop a deep learning-based classification pipeline using nnU-Net and post-processing rules to detect pulmonary embolism (PE) in CTPA with state-of-the-art sensitivity, specificity, and AUROC across internal and external validations.

Background

Computed tomography (CT) pulmonary angiography (CTPA) is a medical imaging technique that uses an intravenous (IV) contrast agent to improve the visibility of thoracic blood vessels, with a particular focus on the pulmonary arteries [17,137]. CTPA is currently the preferred imaging method for diagnosing pulmonary embolism (PE) [58,138]. Beyond PE, cardiovascular disease (CVD) is the primary cause of morbidity and mortality worldwide [139]. Accurate identification and measurement of major blood vessels in the thoracic cavity are critical for radiologists in diagnosing and assessing CVDs [140–142]. CTPA also enhances the visibility of other significant blood vessels within the chest cavity, thereby aiding radiologists in effectively evaluating CVDs [143,144]. Several CVDs, such as chronic thromboembolic pulmonary hypertension (CTEPH), pulmonary arterial hypertension (PAH) [145–147], and aortic aneurysms [148,149], can be identified or suspected based on the presence of enlarged pulmonary arteries or an enlarged ascending aorta [150–152].

During the CTPA reading and reporting process for PE, radiologists manually perform quality control and various measurements of mediastinal structures in the images, depending on the clinical situation and local practices. Measurements of the standard deviation of Hounsfield Units (HU) in a specific region of interest (ROI), such as the descending aorta (DAo), and the mean HU value in the pulmonary trunk (PT), are utilized for image quality assessment [14,153]. The mean HU value in PT aids in selecting the optimal window setting for PE detection [154]. These manual measurements are time-consuming [155], and a fully automated solution could potentially enhance radiologists' workflow efficiency and accuracy, thereby improving overall patient outcomes.

Current automatic methods for segmenting and measuring major blood vessels in the chest cavity typically use traditional image processing and analysis techniques [156–158]. Although deep learning-based approaches have shown potential [159–161], many of the existing datasets are limited by small sample sizes and a lack of representative artifacts and co-morbidities. To address the challenges presented, **Paper I** proposes an algorithm leveraging traditional image processing and analysis techniques, utilizing deterministic methods to accurately segment and measure mediastinal structures specifically the DAo, AAo, PT in CTPA examinations. These validated segmentation outputs were then used as ground truth annotations for training deep learning models. In **Paper II**, we trained a state-of-the-art semantic segmentation framework, the no-new-U-Net (nnU-Net) [130], on the accurately segmented vascular structures from the cohort of **Paper I**. This deep learning approach demonstrated the ability to detect and segment mediastinal structures with high precision. Furthermore, we compared the results of this statistical, probabilistic approach with the deterministic methods of **Paper I**, benchmarking the performance of

the nnU-Net against expert radiologists and highlighting the strengths and potential of each approach in clinical practice.

PE is a critical and potentially fatal condition that arises when blood clots block the pulmonary arteries, leading to significant morbidity and mortality [11]. In Europe alone, over 400,000 individuals are affected by PE [49], with estimates ranging from 300,000 to 600,000 cases annually in the United States, resulting in more than 100,000 deaths each year [50,51]. As one of the leading causes of preventable hospital deaths globally [48], PE demands rapid and effective clinical intervention [162]. CTPA imaging technique involves a CT scan performed after the intravenous administration of iodinated contrast medium, which highlights emboli as dark filling defects within the pulmonary arteries [40]. However, reviewing each CT slice to detect PE is a time-intensive process for radiologists, requiring extensive training and attention to detail. Additionally, small sub-segmental emboli present a challenge due to high inter-observer variability [20]. An automated PE detection system in CTPA can help radiologists by speeding up the reading process and reducing the risk of missing emboli.

Developing an accurate automated solution for PE detection is challenging due to anatomical variations, motion artifacts, variations in contrast medium concentration, and coexisting pathologies. To date, various techniques have been explored, including traditional image processing methods [163,164] and statistical/probabilistic approaches like machine learning [165–167] and deep learning [168,169]. Despite these efforts, these models often struggle with low sensitivity [164,166,168] and high false positive rates [163,164,166,167], primarily due to limited training data [163,164,166–168]. The leading method currently employs a ResNet classification model on 1465 CTPA scans, achieving a sensitivity of 92.7% and specificity of 95.5% [170]. Similarly to **Paper II**, we trained the nnU-Net semantic segmentation model for PE segmentation in **Paper III**. The nnU-Net framework [130] significantly improves segmentation performance, enabling automatic classification of routine patient CTPA examinations as PE-positive or PE-negative with higher sensitivity and specificity than the current state-of-the-art methods.

Materials

Ethical Consideration

A retrospective dataset comprising 700 non-ECG-gated CTPA examinations conducted between 2014 and 2018 at a single institution (Nyköping Hospital, Sweden) was collected. Approval for the collection and analysis of these CTPA examinations was obtained from the Swedish Ethical Review Authority (EPN Uppsala Dnr 2015/023 and 2015/023/1). The CTPA examinations were standard clinical procedures, exported sequentially from a chronological history list within the institution's Picture Archiving and Communication System (PACS) in Digital Imaging and Communications in Medicine (DICOM) format. To ensure anonymization, all personal identifiers within the DICOM headers were removed using the Dicom2USB hardware solution (www.dicom2usb.com).

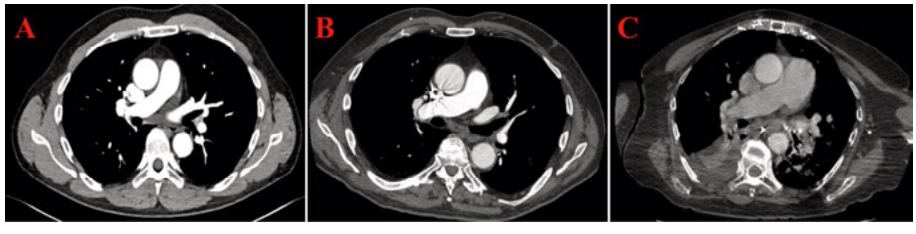

Figure 16. Representative examples of CTPA examinations at the level of PT, showcasing varying image quality. The radiologist categorized these examinations as good, acceptable, or inferior quality. **Panel A** displays a good-quality CTPA exam. **Panel B** presents an acceptable quality CTPA exam, with some image noise and streak artifacts from the superior vena cava. **Panel C** demonstrates an inferior quality CTPA exam characterized by severe image noise, motion artifacts, and inadequate IV contrast concentration in the PT. In all panels, the CTPA exams have the same window setting (width = 600 HU, level = 100 HU).

Assessment of CTPA Volume Image Quality

For each CTPA examination, the radiologist evaluated five image quality parameters that influence the assessment of pulmonary embolism (PE): motion artifacts, streak artifacts, intravenous contrast concentration in the pulmonary trunk (PT), parenchymal disease, and image noise. A total quality score was computed, categorizing the overall CTPA examination quality as good (score 0–3), acceptable (score 4–7), or poor (score ≥8). **Table 3** summarizes the distribution of the CTPA examination dataset across various quality levels with the study characteristics, utilized for training, validation, and testing in **Papers I**, **II**, and **III**. Illustrated examples of three CTPA quality categories are provided in **Figure 16**, with detailed information on the original scoring methodology and calculation outlined in the supplementary material of **Paper I**.

Manual Measurements of Major Blood Vessels

The radiologist measured the diameters of the AAo and PT, the IV contrast concentration in the PT, and the image noise in the 2 mm axial image stack, The PT diameter was measured proximal to the bifurcation point, while the AAo diameter was measured at the level of the PT. For the IV contrast concentration, a 2 cm² circular ROI was placed in the PT to calculate the mean HU value. Similarly, a 1 cm² circular ROI was positioned in the DAo to calculate the SD of HU values, which represents the image noise. An example of these measurements is shown in **Figure 17**.

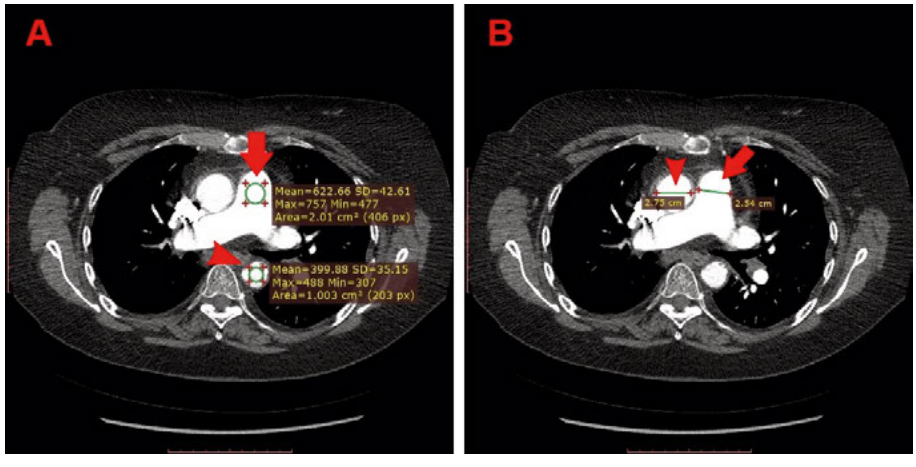

Figure 17. Radiologists carried out the ground truth measurements. **Panel A** shows that the IV contrast concentration in the PT was determined by averaging the HU values within a 2 cm² circular region of interest (indicated by the arrow). The image noise was evaluated by calculating the standard deviation (SD) of the HU in a 1 cm² circular region of interest in the DAo (marked by the arrowhead). **Panel B** depicts the measurements of the PT diameter (arrow) and AAo diameter (arrowhead).

These measurements were performed by an experienced senior radiologist (TF) on the CTPA volume images using the RadiAnt DICOM Viewer (Medixant) (https://www.radiantviewer.com). The initial review and measurements of 150 CTPAs were carried out by a radiology resident (DT) with expertise in general diagnostic radiology, followed by a double-check by radiologist TF. These manual measurements of the major blood vessels were used as the ground truth in **Papers I** and **II** and are provided in **Table 3**.

Table 3. Overview of the Study Cohort from the Internal Dataset.

Characteristics	Paper I		Paper II		Paper III[2]		Overall
	Training Dataset	Test Dataset	Training Dataset	Test Dataset	PE	Non-PE	
No. of patients	170	482	466	186	141	511	652
No. of CTPA exams	180	520	490	210	149	551	700
Sex (Women/Men)	86/84	267/215	245/221	108/78	58/83	295/216	353/299
Median age (IQR) years	72.0 (19.0)	72.0 (18.0)	72.0 (17.0)	74.0 (19.75)	71.0 (17.0)	72.0 (17.5)	72.0 (18.0)
Diseases							
Emboli in (Right/Left) lung	38/35	99/79	100/81	37/33	137/114	0/0	137/114
Pneumothorax in (Right/Left) lung	0/0	4/2	4/2	0/0	1/1	3/1	4/2
Pleural effusion in (Right/Left) lung	66/62	164/152	147/140	83/74	51/46	179/168	230/214
Infiltrate or atelectasis (or other opacities) in (Right/Left) lung	110/92	334/321	298/275	146/138	100/88	344/325	444/413
Pericardial fluid	23	60	57	26	16	67	83
Sign of acute congestive heart failure	33	98	89	42	17	114	131
Lymph nodes (Mediastinum/Right hilum/Left hilum) [1]	24/17/12	114/59/42	90/48/37	48/28/17	27/21/14	111/55/40	138/76/54
Quality of CTPA exams (Good/Acceptable/Inferior)	58/59/63	200/169/151	200/158/132	58/70/82	53/51/45	205/177/169	258/228/214

Note. — Unless otherwise indicated, data are number of examinations. CTPA = computed tomography pulmonary angiography, PE = pulmonary embolism

[1] Lymph nodes larger than 1 cm.

[2] The training dataset for Paper III consists only of patients with PE. Therefore, in this context, the dataset was split into PE and Non-PE cases.

Quantitative Evaluation of Major Blood Vessels Segmentation

In **Paper II**, we used the deterministic solution from **Paper I** to generate 2D segmentation masks, successfully producing segmentation masks for the major blood vessels in 596 out of 700 CTPAs. These masks served as the ground truth for the major blood vessels in the thoracic cavity: the DAo, AAo, and PT. The ground truth segmentation masks were validated by two radiologists, DT and TF. However, the remaining 104 CTPAs required manual annotation, as they could not be processed automatically in **Paper I**. The manual annotations were performed using the open-source software MITK. These annotations for the 104 CTPAs were also validated by radiologists DT and TF to ensure consistency and accuracy.

Manual Annotation of Pulmonary Embolism

In the internal dataset, 149 out of 700 CTPAs showed the presence of PE. These exams were manually segmented in the axial view, image by image, resulting in 36,471 segmentations (**Table 4**). The CTPAs were reviewed and annotated using the open-source software Medical Imaging Interaction Toolkit (MITK) [171] by two radiologists, DT and TF. An example of PE annotation is illustrated in **Figure 18**.

Table 4. Ground truth annotation for 149 internal CTPA scans with PE.

Component	Blood Clots	Average Volume (mm^3)	Min Volume (mm^3)	Max Volume (mm^3)	Total Volume (mm^3)
3D (Volume)	1497	682	0.21	36510	
2D (Area)	36471	16	0.21	830	744783
1D (Voxel)	2439400				

Note. — PE = Pulmonary embolism, 3D = 3-dimensional, 2D = 2-dimensional, 1D = 1-dimensional. Min = minimum, Max = maximum. 3D components comprise 2D components, and 2D components comprise 1D components where a 1D component is equal to 1 voxel.

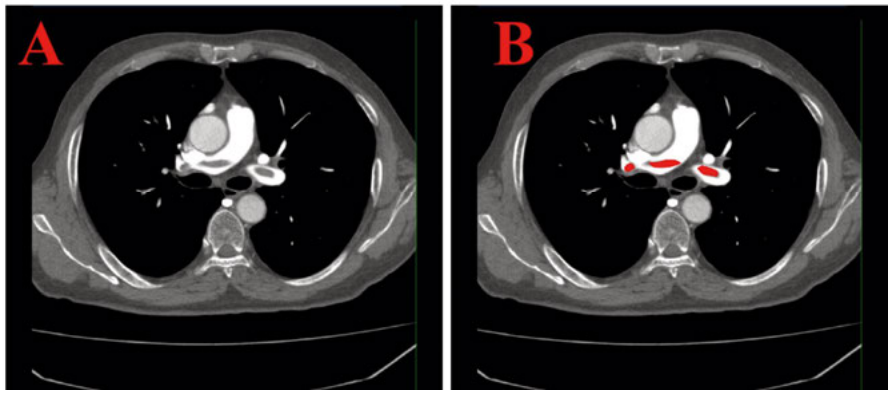

Figure 18. Example of PE annotation. Panel A presents the original CTPA exam, while Panel B displays the radiologist's manual annotation in red. In all panels, the CTPA exams have the same window setting (width = 800 HU, level = 100 HU).

External Datasets

Three publicly available datasets were used to externally evaluate the proposed algorithm and model: the Segmentation of Thoracic Organs at Risk in CT Images (SegTHOR) dataset [172] (used in **Papers I** and **II**), Ferdowsi University of Mashhad's Pulmonary Embolism (FUMPE) Dataset [173] (used in all three papers), and the RSNA-STR Pulmonary Embolism CT (RSPECT) Dataset [174] (used in **Paper III**). The purposes and general outlines of these external datasets are provided below in detail.

Segmentation of Thoracic Organs at Risk in CT images (SegTHOR)

The SegTHOR training set includes 40 CT scans, both with and without IV contrast, all featuring manual segmentation of the aorta [172]. For the external evaluation of AAo segmentation, 12 CT scans with IV contrast were selected from the 40 available scans, while the remaining 28 CT scans without IV contrast were excluded. These 12 CT scans with IV contrast were used for the external validation of AAo segmentation in **Papers I** and **II**.

Ferdowsi University of Mashhad's Pulmonary Embolism Dataset

The FUMPE dataset is a publicly available collection consisting of 35 CTPA examinations with voxel-level PE annotations, including the diameter of the PE annotated by radiologists. The annotation of the PE diameter was used for external evaluation in **Papers I** and **II**, while the voxel-level PE annotations were used for external evaluation in **Paper III**. In the FUMPE dataset, one PE-positive examination was excluded due to the absence of a ground truth annotation. Out of the 34 remaining CTPA examinations, 32 were PE-positive and 2 were PE-negative. Upon reviewing the ground truth, it was found that the annotation mask was incorrect in 8 CTPA examinations. Therefore,

additional corrections were made to these annotations before their use. For further details, please refer to the supplementary materials in **Paper III**.

RSNA-STR Pulmonary Embolism CT (RSPECT) Dataset

The RSPECT dataset comprises a training set (n = 7279) and a test set (n = 2167), with image-level annotations provided for the training set by several radiologists. From the training dataset, 385 CTPAs showing central PE were selected, and an additional 385 CTPAs were randomly chosen from the 4877 CTPAs that did not exhibit PE or other true filling defects. In total, 770 CTPA exams were used for patient-level external evaluation in **Paper III**.

Methodology

Paper I

Automated detection, segmentation and measurement of major vessels and the trachea in CT pulmonary angiography

In **Paper I**, we introduced a Computer-Aided Detection (CADe) system designed to automate the detection, segmentation, and measurement of mediastinal structures, specifically the ascending aorta (AAo), descending aorta (DAo), and pulmonary trunk (PT). This system integrates advanced image processing and analysis techniques to achieve its objectives. The methodology is structured into two primary steps: pre-processing and segmentation. A summary of the details is provided below, and further information can be found in the Supplementary Materials of **Paper I**.

Step 1 Pre-Processing

I. We initially divided an internal set of 700 CTPAs into two groups: a training set (n = 180) for algorithm development, and a test set (n = 520) for unbiased evaluation of the final algorithm.
II. Each axial CT image voxel was converted to Hounsfield Units (HU), and scanning direction was determined using DICOM header information.
III. To account for patient orientation variations due to factors like scoliosis or movement, CT images were aligned along the x-axis of the axial plane from cranial to caudal directions (**Figure 19**, **B**).

Step 2 Segmentation

Step 2.1. Locating Trachea and Bronchial Tree:

I. Two adjoined volumes of interest (VOIs) are extracted from the superior thoracic cavity.
II. Within these VOIs, trachea candidates are identified using thresholding, flood-fill operations, and connected component analyses.
III. The longest candidate meeting empirically determined diameter and volume ranges is selected as the trachea.
IV. The trachea is tracked slice by slice cranially to caudally until the bifurcation point where the left and right main bronchi are distinguished.
V. The CT slice where the distance between bronchi exceeds 0.75 cm is designated as the carina of the trachea (**Figure 19**, **C6**).

Step 2.2. Locating and Measuring the DAo:

I. Detected near the carina of the trachea, posterior to the left main bronchus, based on IV contrast and circularity.
II. Artificial ray search methods identify contrast-filled pixels corresponding to the DAo (**Figure 19**, **C7-9**).
III. The HU density of DAo is calculated using the area of a 1 cm² circle at its mass center (**Figure 19**, **C12**).

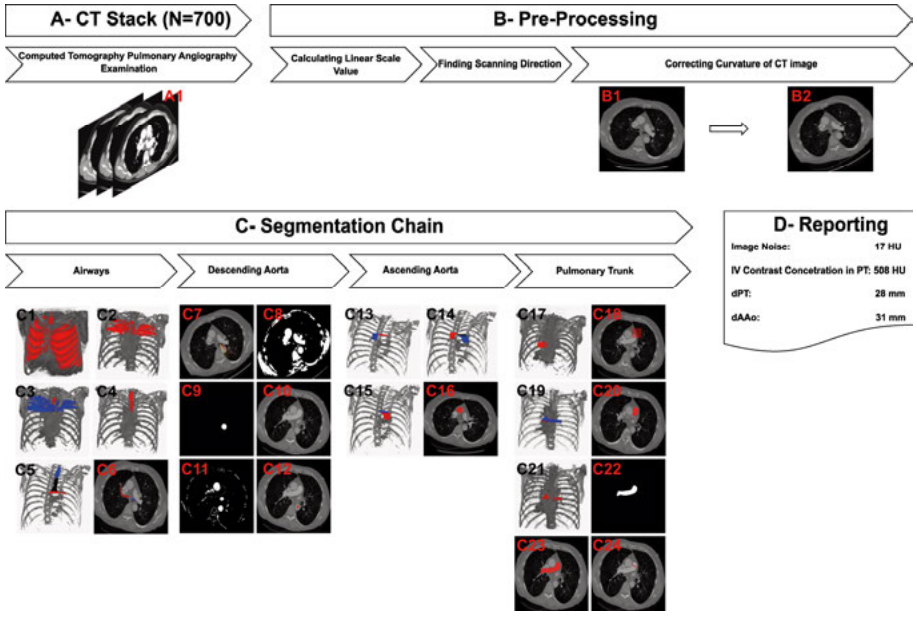

Figure 19. Flowchart of the proposed CADe system. Panel A displays a total of 700 2-mm axial CTPA image stacks retrieved from the PACS server. **Panel B** illustrates the pre-processing stage, where the linear scale values and curvature of the CT images were computed. **Panel C** outlines the segmentation procedure, which consists of four steps, starting with trachea detection, followed by the identification of the DAo, AAo, and PT. **Panel D** emphasizes the system's noise assessment and the reporting of measurements for the mediastinal vascular structures.

Step 2.3. Locating and Measuring the AAo:

I. Identified by tracking segmented DAo regions slice by slice in a caudal-to-cranial direction to detect characteristic morphological changes.
II. The first circular object detected anteriorly in a cranial-to-caudal direction is designated as the AAo (**Figure 19**, **C14**).
III. Segmentation is performed between the levels of the aortic arch and the carina of the trachea to compute the mean diameter of the AAo (**Figure 19**, **C15**).

Step 2.3. Locating and Measuring the AAo:

I. A rectangular search space is created adjacent to the left side of the Aao (**Figure 19**, **C18**).
II. The PT is segmented and tracked cranially to caudally until the proximal part of the PT is identified near the pulmonary valve (PV).
III. The circularity of the segmented region confirms the PV level (**Figure 19**, **C20**).
IV. The PT diameter is calculated using the Hough transform as the mean of diameters across segmented planes (**Figure 19**, **C24**).

Paper II

Segmentation and Measurements of Major Vessels from CT Pulmonary Angiography Using Deep Learning

In **Paper II**, we utilized the deterministic solution from **Paper I** to generate segmentation masks for the AAo, DAo, and PT, which served as the ground truth. The dataset was then divided into a training set of 490 CTPA examinations and a testing set of 210 CTPA examinations. We trained the 2D U-Net architecture with a depth of 7, generated using the nnU-Net framework. For each major vessel (AAo, DAo, and PT), we used 490 2D segmentation masks (**Figure 20, Panel A**). The model was trained separately for each vessel. After training the model, we performed post-processing step followed by a model inference to segment each vessel. A summary of these steps is provided below.

Step 1. Model Inference and Post-Processing:

I. Three trained models were obtained for segmenting the DAo, AAo, and PT (**Figure 20**, **Panel B**).
II. The volume of interest (VOI) was determined by focusing on slices between 22% and 65% of the CTPA volume to capture key anatomical landmarks (**Figure 20**, **Panel C**).
III. The segmentation candidates were processed using deterministic algorithms to identify the best 2D segmentation masks (**Figure 20**, **Panel C**).

Step 2. Descending Aorta (DAo) Segmentation (**Figure 20**, **Panel C**):

I. 3D connected component analysis identified the largest component in the VOI, assuming it to be the DAo.
II. Components smaller than 200 pixels were removed, and a morphological closing operation was performed to refine the boundaries.
III. The standard deviation of Hounsfield Units (HU) within a 1 cm^2 region of interest (ROI) in the DAo was used to measure image noise, with the median value calculated for the final measurement.

Step 3. Ascending Aorta (AAo) Segmentation (**Figure 20**, **Panel C**):

I. The candidate pool was filtered to remove irrelevant small objects, and a 3D connected component analysis was performed.
II. The component with the centroid closest to the superior part of the CTPA was selected.
III. Further operations, including tracking shifts in area and centroid, ensured that the final component represented the AAo.
IV. The equivalent diameter of 2D objects in the final 3D component was measured, and the median value provided the final diameter.

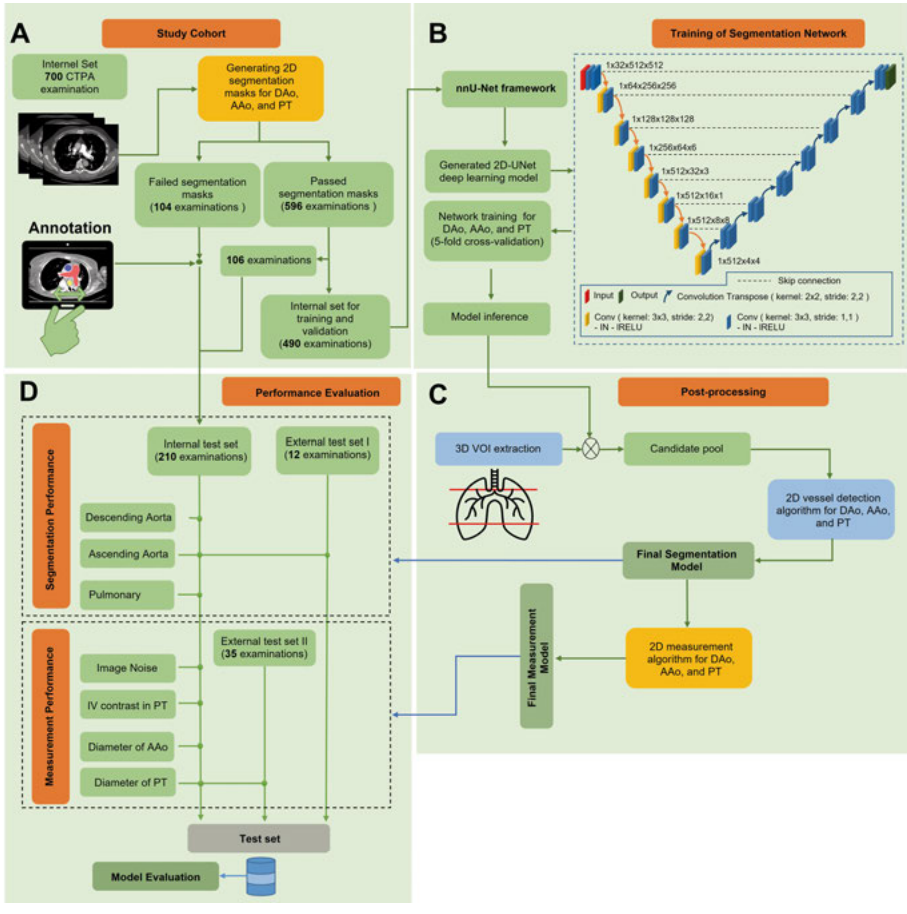

Figure 20. Study design of Paper II. A total of 700 CTPA examinations were collected, and a deterministic segmentation algorithm from Paper I was used to generate 2D masks for the DAo, AAo, and PT. Segmentation was successfully performed on 596 examinations, with 104 requiring manual annotation. The dataset was split into 490 training and 210 testing scans (Panel A). The 2D U-Net model, created using the nnU-Net framework, was trained on 490 scans with 5-fold cross-validation. The model architecture included 3×3 convolutional layers, instance normalization, and leaky ReLU (Panel B). Vessel candidates were generated through model inference, followed by 2D vessel detection and measurement algorithms (Panel C). The final model's performance was evaluated on 210 internal CTPAs and 47 CTPAs from two public datasets (Panel D). Gold-colored boxes represent Paper I solutions, while light blue boxes indicate Paper II contributions.

Step 4. Pulmonary Trunk (PT) Segmentation (**Figure 20**, **Panel C**):

I. Small components were filtered out, and a morphological opening operation removed noise and irrelevant structures.
II. Components with less than 10,000 pixels were discarded, and reference points were established to identify the likely PT.

III. The algorithm prioritized the proximity of components to the reference points, ensuring that the correct component was selected as the PT.
IV. The selected component underwent a closing operation to smooth the boundaries, completing the segmentation.

Step 5. IV Contrast in PT and Measurement (**Figure 20**, **Panel C**):

I. The mean HU of all 2D objects in the final PT component was used to measure the IV contrast concentration.
II. The diameter of the PT was measured using horizontal line segments extracted via the Hough transform, and the median value of these segments provided the final diameter.

Paper III

Enhanced Classification Performance using Deep Learning Based Segmentation for Pulmonary Embolism Detection in CT Angiography.

In **Paper III**, we trained the 3D U-Net architecture, generated using the nnU-Net framework, on PE-positive examinations from the internal dataset (n=149). The data were randomly split into training (80%, n=119) and validation (20%, n=30) sets. We used 5-fold cross-validation during model training. After training and validation, the validated model was embedded in a classification algorithm consisting of three steps: pre-processing, image segmentation inference, and post-processing. These steps are summarized below:

Step 1. Pre-processing:

I. All DICOM data were converted to the NIfTI format using an in-house Python script.

Step 2. Image Segmentation Inference:

I. The trained nnU-Net model was used to perform the segmentation inference of PE (**Figure 21**, **Panel B**).

Step 3. Post-processing:

I. The softmax function in the final layer provides a probability distribution across predicted classes. We developed a set of logical rules based on different softmax probability thresholds (0.75 to 0.95) and volumetric thresholds (0 mm^3 to 200 mm^3) were used to create segmentation masks with varying volumes (**Figure 21**, **Panel C**).
II. The segmentation output was then transformed into patient-level classification by applying a threshold based on the total predicted emboli volume (**Figure 21**, **Panel C**).

III. We developed two distinct strategies. Strategy 1 provided the best balance between sensitivity and specificity, while Strategy 2 delivered the highest specificity (see Supplementary Materials of **Paper III**).

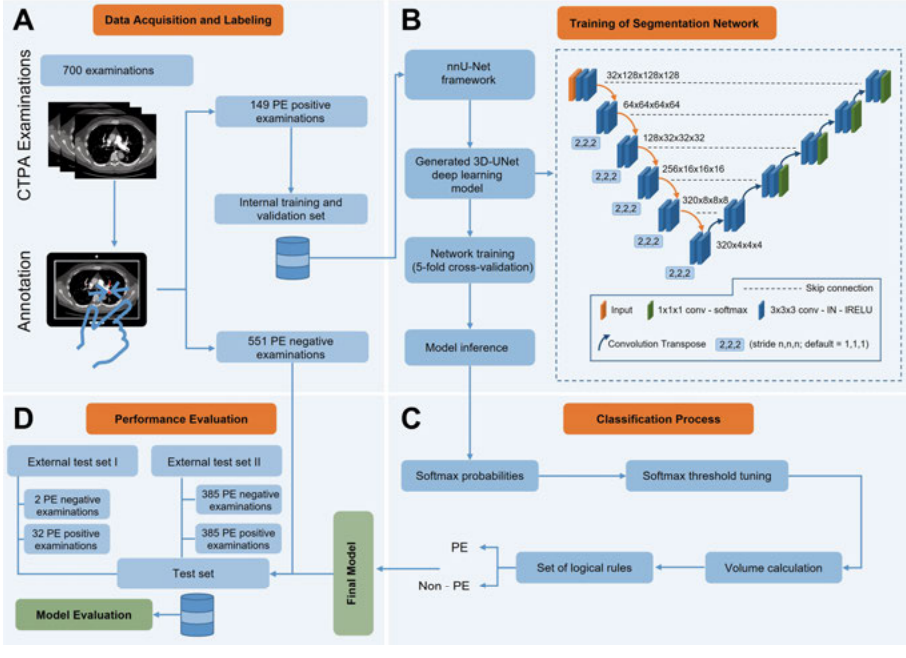

Figure 21. Study design of Paper III. 700 CTPA examinations were annotated by two radiologists, with 149 PE-positive exams used for training and PE-negative exams reserved for evaluation (Panel A). A 3D U-Net model, trained with 149 PE-positive CTPAs using 5-fold cross-validation, utilized a 3×3×3 filter, instance normalization, and leaky ReLU (Panel B). Softmax probabilities were used for voxel classification and predicted PE volume calculation. Patient-level classification was achieved through volume thresholding and logical rules (Panel C). The model was evaluated on 804 external CTPA exams from two public datasets (Panel D).

Results and Discussion

Paper I

Automated detection, segmentation and measurement of major vessels and the trachea in CT pulmonary angiography

A total of 700 CTPA examinations were included in the **Paper I**, conducted on 652 patients (54% women) aged 16–100 years (median 72; interquartile range 18). Ground truth was established by a comprehensive review conducted by a senior radiologist and a radiology resident. Of the total examinations, 180 were randomly designated for training and 520 for testing. A radiologist's quality assessment determined that 65% of the training set and 71% of the test set were rated as good or acceptable, with the remainder was classified as inferior. Nonetheless, all examinations were included in the study.

A fully automated CADe system was developed to detect, segment, and measure critical mediastinal structures, including major vessels (e.g., AAo, DAo, PT) and anatomical landmarks (e.g., tracheal bifurcation). Two radiologists independently evaluated the CADe outputs, achieving high initial inter-observer agreement (99.52%–100%), with any remaining disagreements resolved by consensus. In the test set, correct detection of the tracheal bifurcation and carina was observed in 96% of examinations, while the pulmonary vein (PV)/proximal PT was correctly identified in 87%. Regarding cardiovascular structures, the DAo was detected in 90%, the AAo in 86%, and the PT in 88% of cases. Once identified, these structures were successfully segmented in 100% of the relevant test scans. Examination quality had a mild effect, with good-quality scans generally yielding slightly better detection and measurement performance than inferior-quality ones.

Quantitative comparisons between the CADe system and the radiologist showed strong correlations for image noise (Pearson's $r=0.87$), IV contrast level in the PT ($r=0.99$), AAo diameter ($r=0.92$), and PT diameter ($r=0.68$) ($p<0.001$) (**Figure 22**). Bland-Altman analysis indicated minimal mean differences (e.g., -0.25 HU for image noise, 0.51 mm for AAo diameter) and small percentage differences (-1.08% for image noise, 1.68% for AAo diameter). Although the system performed best in higher-quality scans, it remained robust even when applied to those classified as inferior. When validated externally on 12 CTPAs from the SegTHOR dataset, the AAo segmentation achieved a median Dice score of 0.92, showing notable improvement compared to prior systems that reported an overall median Dice score of 0.82 for multiple cardiovascular structures in smaller datasets [159]. Furthermore, validation in 35 CTPA exams from the FUMPE dataset confirmed a strong correlation ($r=0.83$, $p<0.001$) between the CADe system and radiologist PT diameter measurements.

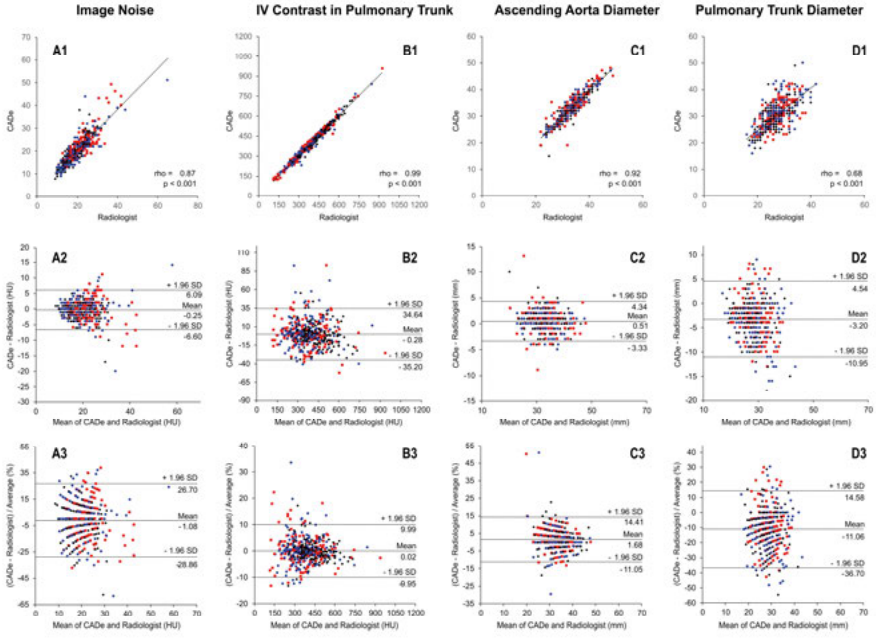

Figure 22. Comparison of the Paper I automated CADe system with radiologist measurements. Top row: regression analysis (dashed lines). Middle row: Bland–Altman plots of radiodensity and diameter differences (limits ±1.96 SD). Bottom row: percentage differences (limits ±1.96 SD). (A) Image noise (n=470), (B) Intravenous contrast agent in PT (n=455), (C) Ascending aorta diameter (n=447), (D) Pulmonary trunk diameter (n=455). Exam quality was rated as good (black diamonds), acceptable (blue circles), or inferior (red squares).

Compared to earlier work that analyzed smaller cohorts [156,159,175], this system was tested on a significantly larger, clinically representative set of CTPAs, many of which had suboptimal image quality. While artifact-induced segmentation errors were more common for the PT, the performance remained high even in inferior scans, emphasizing the system's utility in real-world conditions. Its sequential segmentation approach, which identifies the DAo first, followed by the AAo and PT, enables full automation but makes later steps susceptible to initial detection errors.

In summary, **Paper I** presents a fully automated CADe system that reliably detects, segments, and measures mediastinal landmarks, major vessels, and imaging parameters in CTPA scans. It demonstrates high concordance with radiologist assessments both internally and in external validation, reflecting its potential for routine clinical use. By processing large image datasets quickly and accurately, this approach could not only expedite diagnostic workflows but also facilitate broader research on mediastinal morphology, serving as a foundation for future AI-driven chest CT innovations.

Paper II

Segmentation and Measurements of Major Vessels from CT Pulmonary Angiography Using Deep Learning.

In **Paper II**, the same internal dataset (n=700 CTPAs) used in **Paper I** was utilized. Since **Paper II** is based on a statistical approach, a larger training set size was required. Therefore, a different training and testing split ratio was applied, with the dataset divided into training and testing sets using a 70/30 split. Of the 490 CTPAs selected for training and 5-fold cross-validation, 1,470 corresponding 2D segmentation masks were generated (490 per each of the DAo, AAo, and PT). For testing, 630 2D masks from 210 CTPAs plus 312 manually annotated masks from 104 CTPAs were used, ensuring no overlap between training and testing.

Using a nnU-Net–based deep learning (DL) model [130] combined with a deterministic post-processing step, the algorithm detected all three major vessels (DAo, AAo, and PT) in the 210 internal test CTPAs, with segmentation failures in 3, 8, and 15 cases, respectively. For the successfully segmented vessels, the combined overall median Dice score was 0.95 (IQR 0.05). Specifically, median Dice values of 0.94–0.95 for the DAo, 0.95–0.96 for the AAo, and 0.95–0.96 for the PT were achieved, depending on image quality (good, acceptable, or inferior). External validation of AAo segmentation on 12 contrast-enhanced CT examinations from the SegTHOR dataset [172] yielded a median Dice score of 0.94 (IQR 0.02), a Jaccard index of 0.88 (IQR 0.04), and a Boundary F1 (BF) contour matching score of 1.0.

Measurement analyses were performed on successfully segmented cases. Within the internal test set, image noise correlated strongly with radiologist assessments (Pearson's $r=0.91$, $p<0.001$), as did AAo diameter ($r=0.93$), IV contrast in the PT ($r=0.98$), and PT diameter ($r=0.55$). Mean differences ranged from -0.03 HU for image noise to -2.16 mm for PT diameter, and Bland-Altman analyses showed moderate percentage differences (e.g., 5.56% for AAo diameter, -7.65% for PT diameter) (**Figure 23**). External measurement validation used 35 CTPAs from the FUMPE dataset [173], where PT diameter yielded $r=0.83$ ($p<0.001$) and a mean difference of -1.43 mm (-5.14%) from radiologist annotations.

Compared to the prior automated deterministic approach in **Paper I**, the proposed method in **Paper II** demonstrates higher segmentation success rates for the DAo (99% vs. 90%), AAo (96% vs. 86%), and PT (93% vs. 88%), along with improved accuracy for image noise and PT diameter measurements. However, there is a slightly larger discrepancy in AAo diameter (1.78 mm vs. 0.51 mm) and PT contrast measurements (17.62 HU vs. -0.28 HU). The robust performance of the nnU-Net–based model aligns with other deep learning methods reported in the literature [159,176–178], outperforming many traditional multi-atlas or model-based frameworks [176,179] and

remaining competitive with foundation models (e.g., SAM, MedSAM) [116,117,180].

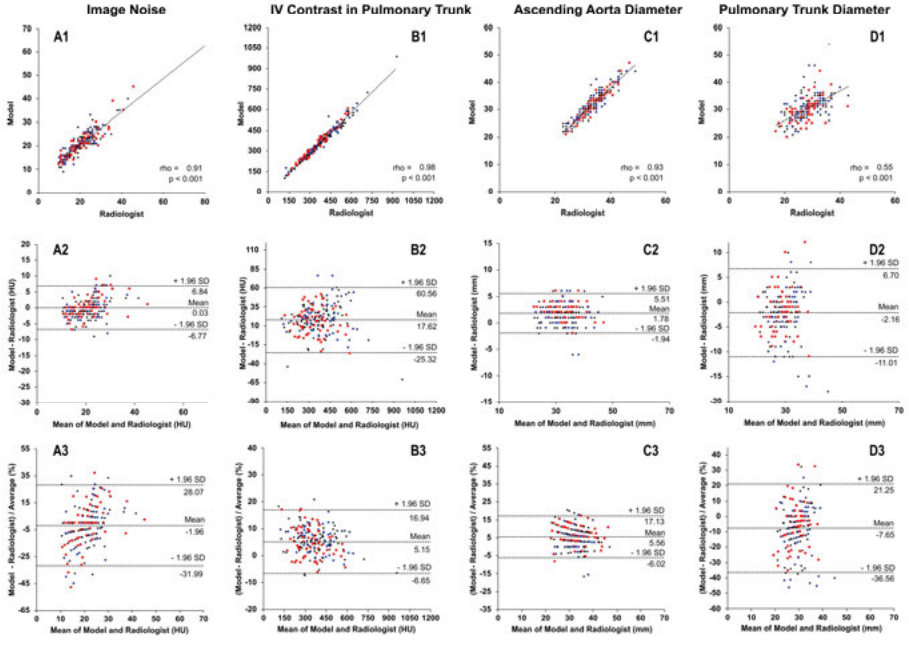

Figure 23. Comparison of the develop model of Paper II with radiologist measurements. Top row: regression analysis (dashed lines). Middle row: Bland–Altman plots of radiodensity and diameter differences (limits ±1.96 SD). Bottom row: percentage differences (limits ±1.96 SD). (A) Image noise (n=207), (B) Intravenous contrast agent in PT (n=195), (C) Ascending aorta diameter (n=202), (D) Pulmonary trunk diameter (n=195). Exam quality was rated as good (black diamonds), acceptable (blue circles), or inferior (red squares).

In conclusion, **Paper II** presents an automated, end-to-end DL-based system that accurately segments major chest vessels and provides strongly correlated measurements relative to radiologist annotations. Although a deterministic post-processing step led to a few segmentation failures, mostly related to suboptimal image quality, the method generally performed reliably on both internal and external datasets. The demonstrated improvements over the deterministic approach in **Paper I** confirm the potential clinical utility of integrating these automated tools into routine workflows, such as PACS, to streamline measurements of key vascular structures in CTPA examinations.

Paper III

Enhanced Classification Performance using Deep Learning Based Segmentation for Pulmonary Embolism Detection in CT Angiography.

Paper III presents the development and evaluation of an automated algorithm for classifying PE in CTPA examinations using a deep learning framework, nnU-Net. A total of 2,439,000 voxels from 1497 PE instances were annotated in the internal dataset, encompassing both acute and chronic PEs without differentiation. The model was trained using a five-fold cross-validation strategy, employing 119–120 training and 29–30 validation CTPAs per fold. Performance evaluation excluded 21 examinations with small PEs (volume < 50 mm^3) and utilized the remaining 128 PE-positive and 551 PE-negative cases.

On the internal dataset, the model achieved a Matthews correlation coefficient (MCC) of 84.9% using a 20 mm^3 threshold volume with post-processing, correctly identifying 96.1% of PE-positive cases and 94.6% of PE-negative cases. External validation on the FUMPE dataset (34 PE-positive and 2 PE-negative cases) achieved an AUROC of 98.5%, sensitivity of 96.9%, and specificity of 100%. Similarly, in the RSPECT dataset (385 PE-positive and 385 PE-negative cases), the model achieved an MCC of 88.6%, an AUROC of 98.6%, sensitivity of 98.4%, and specificity of 89.9% (**Table 5**). Increasing the threshold volume to 50 mm^3 optimized specificity, achieving 96.7% on the internal dataset and 100% and 96.9% on the FUMPE and RSPECT datasets, respectively.

Compared to traditional and contemporary methods, the proposed nnU-Net-based model outperformed previous approaches in sensitivity, specificity, and overall classification accuracy. Earlier methods, such as those by Maizlin et al. [181], Wittenberg et al. [20,182], and Lahiji et al. [183], demonstrated significant limitations, including low specificity (21–26.9%) and inconsistent sensitivity (53.3–97.5%). Deep learning-based approaches like those of Tajbakhsh et al. [184], Rajan et al. [169], and Huang et al. [185] achieved AUROCs of 70–85% but were constrained by small test datasets and limited specificity. The nnU-Net surpassed the state-of-the-art ResNet-based system by Weikert et al. [170] (sensitivity of 92.7% and specificity of 95.5%) by achieving 96.2% sensitivity and 96.8% specificity on a combined test set of 1355 examinations.

Post-processing strategies proved essential for balancing sensitivity and specificity. Strategy 1 optimized this trade-off, while Strategy 2 prioritized specificity, reducing false positives caused by low contrast medium or structures outside the thoracic cavity. False negatives were primarily associated with chronic PEs, highlighting a need for further refinement. Additionally, setting a cut-off volume of 50 mm^3 excluded small, often ambiguous PEs, reducing inter-observer variability and improving consistency in model performance.

Table 5. Diagnostic performance of the trained model.

Parameter	With the Post-Processing		
	Internal Dataset	FUMPE External Dataset	RSNA External Dataset
No. of CTPAs	679	34	770
No. of TN	521	2	346
No. of FP	30	0	39
No. of TP	123	31	379
No. of FN	5	1	6
MCC (%)	84.9	80.4	88.6
Sensitivity (%)	96.1 (91-98)	96.9 (84-99)	98.4 (97-99)
Specificity (%)	94.6 (92-96)	100 (34-100)	89.9 (86-93)
Accuracy (%)	94.8	97.1	94.2
Balanced Accuracy (%)	95.4	98.4	94.2
AUC (%)	96.4	98.5	98.6

Note. — The threshold volume is set to 20 mm^3. Data in parentheses are 95% CIs in percentages. CTPAs = computed tomography (CT) pulmonary angiography (CTPA) examinations, TN = true-negative CTPAs, FP = false-positive CTPAs, TP = true-positive CTPAs, FN = false-negative CTPAs, MCC = Matthew's correlation coefficient, AUC = area under the receiver operating characteristic curve.

In summary, the proposed method in **Paper III** demonstrates substantial clinical utility in PE detection, offering reliable classification and aiding radiologists by prioritizing positive cases. This method represents a significant advancement in automated PE diagnosis, with potential to enhance diagnostic accuracy and workflow efficiency. However, further improvements in sensitivity and specificity are warranted to fully realize its clinical potential.

Conclusion and Future Perspectives

The increasing number of examinations requiring interpretation by radiologists presents a significant challenge for the healthcare system [7,8]. Automated systems designed to perform precise detection, segmentation, and measurement tasks in CT imagery offer a potential solution; however, their current performance levels remain inadequate for routine clinical use. This thesis focuses on developing and evaluating two types of models: deterministic models utilizing conventional image processing and analysis techniques, and probabilistic/statistical models leveraging deep learning architectures. These models are designed to automatically detect PE, segment, and measure mediastinal structures in non-ECG-gated CTPA scans.

In **Paper I**, we presented a deterministic system for detecting and segmenting major blood vessels in CTPA examinations. In contrast to commonly used probabilistic techniques, such as CNNs that depend on detailed pixel-level labels for segmentation tasks, our method avoids the need for manual pixel-wise annotations altogether. This key feature eliminates the dependency on expert-level annotations during model development, marking a significant contribution to the field. Moreover, the deterministic model offers inherent transparency, allowing all segmentation or measurement errors and unexpected outcomes to be easily traced and understood. This addresses the "black box" issue often associated with probabilistic approaches, enhancing both reliability and interpretability.

The developed deterministic system demonstrated promising performance across various CTPA image quality levels. However, its reliance on over-parameterized models during the extensive development phases presents a significant drawback, requiring considerable time and effort. This challenge underscores the complexity of many computer vision tasks in medical imaging, which are often categorized as ill-posed inverse problems [186]. These issues, including detecting and segmenting vascular structures or identifying PE in CTPA volume images, exceed the capabilities of traditional image processing techniques. To overcome these limitations, deep learning techniques offer a powerful solution for tackling these ill-posed problems [187]. In **Papers II** and **III**, we leveraged deep learning methods to effectively address the challenge of detecting and segmenting major blood vessels and PE detection in CTPA volume images, bypassing the shortcomings of conventional approaches.

In **Paper I**, the measurement of PT diameter had a Pearson's rho value of 0.68, while in **Paper II**, it was 0.55 in the internal test dataset. This indicates

a need for a more robust PT diameter measurement algorithm. We plan to enhance the PT diameter measurement algorithm in the future to improve the correlation between the CAD system and radiologists. In **Paper III**, the classification performance of the trained deep learning model (nnU-Net) was assessed using 770 CTPA scans randomly selected from the RSNA Pulmonary Embolism CT Dataset, with an equal distribution of PE (n=385) and non-PE cases (n=385). The RSNA training dataset, however, comprises a total of 7,279 CTPA examinations, including 2,368 PE cases and 4,911 non-PE cases. To enhance the external testing performance, we plan to evaluate the model on the entire RSNA dataset in the future. Additionally, a radiologist review will be conducted on selected RSNA CTPA scans.

To maximize the potential of the models presented in this thesis, their integration into the PACS server is essential. A straightforward approach to achieve this is by creating Grey Scale Presentation State (GSPS) objects to encapsulate the detection, segmentation and measurement results. This integration would enable seamless analysis of the GSPS objects using any universal image viewer available on the PACS server, thereby making it easier to test the proposed models in a clinical setting. In our future work, we aim to develop the necessary functionalities for generating GSPS objects to support this process effectively.

The ratio of left ventricle (LV) to right ventricle (RV) diameters serves as a key indicator of right ventricular enlargement and is associated with right ventricular dysfunction, pulmonary hypertension, and PE [188]. A fully automated CAD system capable of accurately measuring the RV/LV diameter ratio could significantly benefit both research and clinical workflows. In our ongoing study, we have developed a fully automated deterministic algorithm to identify the left and right ventricles in CTPA volume images. Preliminary results demonstrate successful localization of the ventricles in a training set of 174 CTPA examinations. Further evaluation of ventricular segmentation and diameter measurements will be conducted on the complete internal dataset of 700 CTPA examinations. Furthermore, additional structures can offer valuable prognostic insights or act as diagnostic indicators. For instance, volumetric analysis of heart chambers [189] or the assessment of contrast reflux into the inferior vena cava [190] can be evaluated in CTPA scans. We plan to incorporate these segmentation and measurement capabilities into a future project to enhance diagnostic and prognostic precision.

There are additional areas of research that warrant further investigation in the future. In **Papers II** and **III**, we employed the state-of-the-art semantic segmentation framework nnU-Net for major vessel and PE detection. However, alternative architectures, such as vision transformers [111,191] and Kolmogorov-Arnold Networks (KANs) [192], may offer improved accuracy and performance. As part of our future work, we plan to train and evaluate these architectures on our internal dataset to compare their performance with the models proposed in this thesis.

Populärvetenskaplig Sammanfattning

Datortomografisk Pulmonell Angiografi (CTPA) är en viktig avbildningsteknik inom sjukvården som gör det möjligt att identifiera livshotande tillstånd såsom lungemboli och hjärt-kärlsjukdomar. Lungemboli uppstår när blodproppar blockerar lungartärerna, vilket kan leda till allvarliga komplikationer eller till och med död om det inte behandlas. Hjärt- och kärlsjukdomar är den ledande dödsorsaken globalt. Även om CTPA är effektivt för att upptäcka dessa tillstånd är analysen av bildmaterialet en arbetsintensiv och komplex process där radiologer manuellt måste mäta och utvärdera strukturer i brösthålan. Det är en uppgift som kan vara tidskrävande, benägen att drabbas av mänskliga fel och en utmaning p.g.a. den ökande arbetsbelastningen inom den moderna sjukvården.

Denna avhandling undersöker möjligheterna till automation för att hantera dessa utmaningar genom att utveckla avancerade datoralgoritmer som kan hitta, mäta och analysera kritiska strukturer i bilder från CTPA-undersökningar. Genom att integrera traditionella bildbehandlingstekniker med banbrytande artificiell intelligens (AI) är målet att göra den diagnostiska processen snabbare, mer exakt och konsekvent. Forskningen belyser den transformativa roll som automation kan spela inom radiologi genom att minska belastningen på vårdpersonal och samtidigt förbättra för patienterna.

Det första steget i forskningen var skapandet av en deterministisk algoritm som kan segmentera stora blodkärl, inklusive uppåtstigande aorta, nedåtgående aorta, och lungartärstammen. Den utvecklade algoritmen visade sig vara både noggrann och tillförlitlig och matchade de manuella mätningar som gjorts av radiologer. En viktig egenskap var att den inte krävde manuellt annoterad data för träning, vilket gör den till en praktisk lösning för omedelbara kliniska tillämpningar. Detta arbete visade att det är möjligt att automatisera rutinmässiga segmenteringsuppgifter i CTPA-undersökningar och lade grunden för ytterligare utveckling.

Baserat på denna grund användes i nästa steg djupinlärning, en typ av maskininlärning, för att förbättra segmenteringsprocessens prestanda. En toppmodern modell för neurala nätverk, kallad nnU-Net, tränades på data från den deterministiska algoritmen, vilket ledde till avsevärd förbättring av segmenteringsnoggrannheten med prestandamått över 95%. Den djupinlärningsbaserade modellen överträffade inte bara traditionella metoder utan visade också robusthet över variationsrika dataset, vilket ger ökad potential för klinisk

användning. Genom att utnyttja styrkorna hos både deterministiska och probabilistiska tillvägagångssätt ökade denna forskning möjligheterna för automatiserad segmentering inom medicinsk bildbehandling.

Det sista området i avhandlingen fokuserade på att automatiskt identifiera lungemboli, ett kritiskt tillstånd som kräver snabb diagnos och behandling. Genom att använda avancerade djupinlärningstekniker utvecklade vi en modell som kunde identifiera lungemboli i CTPA-bilder med högre känslighet och specificitet än många befintliga metoder. Modellens prestanda validerades på externa dataset, där den uppvisade en utmärkt förmåga att generalisera över olika patientpopulationer. Dessa resultat understryker potentialen för AI-drivna verktyg att stödja radiologer i att göra snabbare och korrekta diagnoser.

Automatisering av analysen av CTPA-bilder erbjuder många fördelar. Den påskyndar diagnostikprocessen avsevärt, vilket gör det möjligt för läkare att fatta snabbare beslut för tillstånd som kräver akut handläggning, såsom lungemboli. Genom att minska variationen mellan individuella radiologer säkerställer automatiserade system konsekventa och pålitliga resultat, vilket förbättrar den övergripande diagnostiska noggrannheten. Dessutom frigör dessa system radiologer från rutinuppgifter, vilket gör det möjligt för dem att fokusera på mer komplexa fall och därigenom öka effektiviteten i vårdflödena.

Trots de lovande resultaten kvarstår utmaningar med att integrera dessa system i vardaglig klinisk praxis. Faktorer som variationer i bildkvalitet, skillnader i patientanatomi och behovet av integration med befintlig medicinsk programvara måste hanteras. Framtida forskning kommer att fokusera på att finslipa dessa modeller, utforska mer avancerade AI-arkitekturer som "vision transformers" och utöka deras kapacitet till att mäta ytterligare diagnostiska indikatorer, såsom hjärtkammarvolymer eller ventrikulära dimensioner. Att integrera dessa automatiserade verktyg i bild- och kommunikationssystem (PACS) blir också ett avgörande steg för att underlätta införande på sjukhus och kliniker.

Denna forskning representerar en betydande milstolpe på vägen mot automatiserad medicinsk bildbehandling. Genom att kombinera traditionella bildbehandlingstekniker med modern AI visar avhandlingen hur teknologin kan revolutionera radiologiområdet. Dessa innovationer har potentialen att förbättra för patienterna, minska vårdbördan och bana väg för mer effektiva och tillgängliga diagnostiska verktyg. När vårdsystemet fortsätter att möta ökande krav erbjuder automatisering en lovande lösning för att säkerställa snabb och noggrann vård för alla.

Acknowledgements

First and foremost, I would like to express my profound gratitude to my main supervisor, **Tobias Sjöblom**, for granting me the opportunity to embark on this remarkable doctoral journey. His guidance, expertise, and support have been invaluable throughout the course of my thesis work, and I am deeply thankful for the trust he placed in me.

I am sincerely grateful to **Tomas Fröding** for meticulously preparing the exceptional dataset that formed the backbone of this research. His unwavering assistance, insightful feedback, and dedication were instrumental in overcoming numerous challenges, and I am fortunate to have collaborated with him.

I owe a special debt of gratitude to my co-supervisor, **Christian Jamtheim Gustafsson**, whose extraordinary contributions enriched my thesis immensely. His insightful guidance, thoughtful suggestions, and encouragement were pivotal to the success of this work.

I would also like to extend my heartfelt thanks to **Dimitrios Toumpanakis**, not only for his valuable contributions as a co-author but also for his unwavering friendship. His collaboration brought unique perspectives and depth to my work, and I am truly fortunate to have him as both a colleague and a friend.

A sincere thank you is also due to **Artur Mezheyeuski**, both for his contributions as a co-supervisor and for being a supportive and dependable friend. His encouragement and camaraderie have made this journey all the more enjoyable.

I would also like to thank to my former co-supervisor, **Nataša Sladoje**, for her positive and impactful contributions to the first paper.

I am also indebted to **Chatarina Larsson** for her assistance with my paper I.

I express my deepest gratitude to my dear friend **Margus Veanes** for proofreading my thesis.

Special thanks are due to the **Rudbecklaboratoriet janitorial** team for their tireless efforts in maintaining an efficient and conducive working environment.

I would also like to thank the **Rudbecklaboratoriet IT** department for providing and maintaining the technical infrastructure. Similarly, my gratitude extends to the **Rudbecklaboratoriet Administration** for their invaluable help with administrative tasks.

I would like to thank the former and current members of the Sjöblom group: **Anders, Anna, Chatarina, Emma L., Emma S., Emma T., Israa, Ivaylo, Jim, Joakim, Jordan, Klara, Linnéa, Lucia, Luis, Margus, Natallia, Sudipta, Xiaonan** and **other students** for their contributions to this enriching environment.

I consider it my duty to convey my boundless affection to my cherished ***family*** and ***friends***.

Thank you to **Analytic Imaging Diagnostics Arena** (AIDA) for supporting the work in this thesis through a grant awarded to **Tobias Sjöblom**. Financial support for **Tomas Fröding** and **Dimitrios Toumpanakis** was provided by **AIDA** clinical fellowships, with additional funding for **Tomas Fröding** from the Centre for Clinical Research Sörmland, Uppsala University.

Finally, I am profoundly and eternally grateful to **Stanley Kubrick** and **Rodney William Whitaker**, whose works have illuminated my intellectual and creative world. Their artistry and philosophy have inspired me in countless ways, shaping my perspective to world.

"Never judge a book by its cover"

References

1. Hricak H, Abdel-Wahab M, Atun R, et al. Medical imaging and nuclear medicine: a Lancet Oncology Commission. *The Lancet Oncology*. 2021;22(4):e136-e172.
2. Shung KK, Smith MB, Tsui BM. *Principles of Medical Imaging*. Academic Press; 2012.
3. Kwan AC, Pourmorteza A, Stutman D, Bluemke DA, Lima JA. Next-generation hardware advances in CT: Cardiac applications. *Radiology*. 2021;298(1):3-17.
4. Virani SS, Alonso A, Aparicio HJ, et al. Heart disease and stroke statistics—2021 update: a report from the American Heart Association. *Circulation*. 2021;143(8):e254-e743.
5. McDonald RJ, Schwartz KM, Eckel LJ, et al. The effects of changes in utilization and technological advancements of cross-sectional imaging on radiologist workload. *Academic radiology*. 2015;22(9):1191-1198.
6. Lantsman CD, Barash Y, Klang E, Guranda L, Konen E, Tau N. Trend in radiologist workload compared to number of admissions in the emergency department. *European Journal of Radiology*. Published online 2022:110195.
7. OECD. *Health at a Glance 2023: OECD Indicators*. OECD; 2023. doi:10.1787/7a7afb35-en
8. Clinical radiology census reports | The Royal College of Radiologists. Accessed December 12, 2024. https://www.rcr.ac.uk/news-policy/policy-reports-initiatives/clinical-radiology-census-reports/
9. Bruls RJM, Kwee RM. Workload for radiologists during on-call hours: dramatic increase in the past 15 years. *Insights into Imaging*. 2020;11(1):1-7.
10. Nakajima Y, Yamada K, Imamura K, Kobayashi K. Radiologist supply and workload: international comparison. *Radiation medicine*. 2008;26(8):455-465.
11. Sista AK, Kuo WT, Schiebler M, Madoff DC. Stratification, Imaging, and Management of Acute Massive and Submassive Pulmonary Embolism. *Radiology*. 2017;284(1):5-24. doi:10.1148/radiol.2017151978
12. Renapurkar RD, Shrikanthan S, Heresi GA, Lau CT, Gopalan D. Imaging in Chronic Thromboembolic Pulmonary Hypertension. *Journal of Thoracic Imaging*. 2017;32(2):71-88. doi:10.1097/RTI.0000000000000256
13. Meinel FG, Nance JW, Schoepf UJ, et al. Predictive Value of Computed Tomography in Acute Pulmonary Embolism: Systematic Review and Meta-analysis. *The American Journal of Medicine*. 2015;128(7):747-759.e2. doi:10.1016/j.amjmed.2015.01.023
14. Abadi E, Sanders J, Samei E. Patient-specific quantification of image quality: An automated technique for measuring the distribution of organ Hounsfield units in clinical chest CT images. *Medical physics*. 2017;44(9):4736-4746.

15. Wittenberg R, Peters JF, Weber M, et al. Stand-alone performance of a computer-assisted detection prototype for detection of acute pulmonary embolism: a multi-institutional comparison. *BJR*. 2012;85(1014):758-764. doi:10.1259/bjr/26769569
16. Kang DK, Ramos-Duran L, Schoepf UJ, et al. Reproducibility of CT Signs of Right Ventricular Dysfunction in Acute Pulmonary Embolism. *American Journal of Roentgenology*. 2010;194(6):1500-1506. doi:10.2214/AJR.09.3717
17. Konstantinides SV, Meyer G, Becattini C, et al. 2019 ESC Guidelines for the diagnosis and management of acute pulmonary embolism developed in collaboration with the European Respiratory Society (ERS): The Task Force for the diagnosis and management of acute pulmonary embolism of the European Society of Cardiology (ESC). *European Heart Journal*. 2020;41(4):543-603. doi:10.1093/eurheartj/ehz405
18. Zuin M, Overvad TF, Albertsen IE, Bilato C, Piazza G. Trends of Pulmonary Embolism-Related Sudden Cardiac Death in the United States, 1999–2019. *J Thromb Thrombolysis*. 2024;57(3):483-491. doi:10.1007/s11239-024-02946-7
19. Brunton N, McBane R, Casanegra AI, et al. Risk Stratification and Management of Intermediate-Risk Acute Pulmonary Embolism. *JCM*. 2024;13(1):257. doi:10.3390/jcm13010257
20. Wittenberg R, Peters JF, Sonnemans JJ, Prokop M, Schaefer-Prokop CM. Computer-assisted detection of pulmonary embolism: evaluation of pulmonary CT angiograms performed in an on-call setting. *Eur Radiol*. 2010;20(4):801-806. doi:10.1007/s00330-009-1628-7
21. Dally WJ, Keckler SW, Kirk DB. Evolution of the Graphics Processing Unit (GPU). *IEEE Micro*. 2021;41(6):42-51. doi:10.1109/MM.2021.3113475
22. UNSCEAR 2020/2021 Report Volume I. United Nations : Scientific Committee on the Effects of Atomic Radiation. Accessed September 18, 2023. //www.unscear.org/unscear/en/publications/2020_2021_1.html
23. Esteva A, Robicquet A, Ramsundar B, et al. A guide to deep learning in healthcare. *Nat Med*. 2019;25(1):24-29. doi:10.1038/s41591-018-0316-z
24. Shoshan Y, Bakalo R, Gilboa-Solomon F, et al. Artificial Intelligence for Reducing Workload in Breast Cancer Screening with Digital Breast Tomosynthesis. *Radiology*. Published online 2022:211105.
25. Dembrower K, Wåhlin E, Liu Y, et al. Effect of artificial intelligence-based triaging of breast cancer screening mammograms on cancer detection and radiologist workload: a retrospective simulation study. *The Lancet Digital Health*. 2020;2(9):e468-e474.
26. Kudzinskas A, Callahan AL. Anatomy, Thorax. In: *StatPearls*. StatPearls Publishing; 2024. Accessed December 20, 2024. http://www.ncbi.nlm.nih.gov/books/NBK557710/
27. *"OLI - Drawing Pulmonary Bronchi, Veins and Arteries - English Labels" at AnatomyTOOL.Org by Open Learning Initiative, License: Creative Commons Attribution-NonCommercial-ShareAlike*.
28. Koshi DR. The Cavity of the Thorax. In: *Cunningham's Manual of Practical Anatomy, Volume 2: Thorax and Abdomen, 16th Edition*. Oxford University Press; 2017. Accessed December 24, 2024. accessmedicine.mhmedical.com/content.aspx?aid=1207602759
29. Human Anatomy Atlas (Version v2017.1.27) [Computer software]. (2017). Accessed December 20, 2024. www.visiblebody.com

30. Hall S, Stephens J. The respiratory system. In: Hall S, Stephens J, eds. *Crash Course Anatomy and Physiology*. ; 2019:89-116. doi:10.1016/B978-0-7020-7375-5.00004-3
31. Standring Susan. Great vessels. In: *Gray's Anatomy*. ; 2021:1097-1102.e2. doi:10.1016/B978-0-7020-7705-0.00058-6
32. Stoddard N, Heil JR, Lowery DR. *Anatomy, Thorax, Mediastinum*. StatPearls Publishing, Treasure Island (FL); 2023. http://europepmc.org/abstract/MED/30969641
33. LeVine H. *Medical Imaging*. 1st ed. ABC-CLIO; 2010. doi:10.5040/9798400684333
34. Mikla VI, Mikla VV. *Medical Imaging Technology*. Academic Press; 2014.
35. Wormanns D. Diagnostic Imaging of the Chest. In: Thieme Medical Publishers, Incorporated; 2020.
36. Bushberg JT, Seibert JA. *The Essential Physics of Medical Imaging Study Guide*. First edition. Wolters Kluwer; 2023.
37. Jan J. *Medical Image Processing Reconstruction and Analysis : Concepts and Methods*. Second edition. CRC Press; 2019.
38. *By This W3C-Unspecified Vector Image Was Created with Inkscape . - My Own Work, Converted to Vector Version from Human Male Athletic Model by Nick Zuccarello Posed Using BlenRig Extension and Rendered with Blender., CC BY 3.0, Https://Commons.Wikimedia.Org/w/Index.Php?Curid=4175828*.
39. Henes FOG, Groth M, Begemann PG, Adam G, Regier M. Intraindividual comparison of gadolinium-and iodine-enhanced 64-slice multidetector CT pulmonary angiography for the detection of pulmonary embolism in a porcine model. *Emergency radiology*. 2011;18(3):189-195.
40. Hendriks BMF, Eijsvoogel NG, Kok M, Martens B, Wildberger JE, Das M. Optimizing Pulmonary Embolism Computed Tomography in the Age of Individualized Medicine: A Prospective Clinical Study. *Invest Radiol*. 2018;53(5):306-312. doi:10.1097/RLI.0000000000000443
41. Ahuja J, Palacio D, Jo N, et al. Pitfalls in the imaging of pulmonary embolism. In: *Seminars in Ultrasound, CT and MRI*. Elsevier; 2022.
42. Leitman EM, McDermott S. Pulmonary arteries: imaging of pulmonary embolism and beyond. *Cardiovascular Diagnosis and Therapy*. 2019;9(Suppl 1):S37.
43. Duffett L, Castellucci LA, Forgie MA. Pulmonary embolism: update on management and controversies. *bmj*. 2020;370.
44. Goldhaber SZ, Bounameaux H. Pulmonary embolism and deep vein thrombosis. *The Lancet*. 2012;379(9828):1835-1846.
45. Giordano NJ, Jansson PS, Young MN, Hagan KA, Kabrhel C. Epidemiology, pathophysiology, stratification, and natural history of pulmonary embolism. *Techniques in vascular and interventional radiology*. 2017;20(3):135-140.
46. Moore AJ, Wachsmann J, Chamarthy MR, Panjikaran L, Tanabe Y, Rajiah P. Imaging of acute pulmonary embolism: an update. *Cardiovascular diagnosis and therapy*. 2018;8(3):225.
47. Giri J, Sista AK, Weinberg I, et al. Interventional therapies for acute pulmonary embolism: current status and principles for the development of novel evidence: a scientific statement from the American Heart Association. *Circulation*. 2019;140(20):e774-e801.
48. Jha AK, Larizgoitia I, Audera-Lopez C, Prasopa-Plaizier N, Waters H, Bates DW. The global burden of unsafe medical care: analytic modelling of observational studies. *BMJ Qual Saf*. 2013;22(10):809-815. doi:10.1136/bmjqs-2012-001748

49. Raskob GE, Angchaisuksiri P, Blanco AN, et al. Thrombosis: A Major Contributor to Global Disease Burden. *ATVB*. 2014;34(11):2363-2371. doi:10.1161/ATVBAHA.114.304488
50. Elenizi K, Alharthi R, Galinier M. Pulmonary embolism originating from germ cell tumor causes severe left ventricular dysfunction in a healthy young adult with full recovery: a case report. *BMC Cardiovasc Disord*. 2021;21(1):260. doi:10.1186/s12872-021-02066-7
51. Sista AK, Horowitz JM, Tapson VF, et al. Indigo Aspiration System for Treatment of Pulmonary Embolism. *JACC: Cardiovascular Interventions*. 2021;14(3):319-329. doi:10.1016/j.jcin.2020.09.053
52. Kline JA. Diagnosis and Exclusion of Pulmonary Embolism. *Thrombosis Research*. 2018;163:207-220. doi:10.1016/j.thromres.2017.06.002
53. Stein PD, Beemath A, Matta F, et al. Clinical Characteristics of Patients with Acute Pulmonary Embolism: Data from PIOPED II. *The American Journal of Medicine*. 2007;120(10):871-879. doi:10.1016/j.amjmed.2007.03.024
54. Wells P, Anderson D, Rodger M, et al. Derivation of a Simple Clinical Model to Categorize Patients Probability of Pulmonary Embolism: Increasing the Models Utility with the SimpliRED D-dimer. *Thromb Haemost*. 2000;83(03):416-420. doi:10.1055/s-0037-1613830
55. Le Gal G, Righini M, Roy PM, et al. Prediction of Pulmonary Embolism in the Emergency Department: The Revised Geneva Score. *Ann Intern Med*. 2006;144(3):165. doi:10.7326/0003-4819-144-3-200602070-00004
56. Coelho J, Divernet-Queriaud M, Roy PM, Penaloza A, Le Gal G, Trinh-Duc A. Comparison of the Wells score and the revised Geneva score as a tool to predict pulmonary embolism in outpatients over age 65. *Thrombosis Research*. 2020;196:120-126. doi:10.1016/j.thromres.2020.07.026
57. Kline JA, Courtney DM, Kabrhel C, et al. Prospective multicenter evaluation of the pulmonary embolism rule-out criteria. *Journal of Thrombosis and Haemostasis*. 2008;6(5):772-780. doi:10.1111/j.1538-7836.2008.02944.x
58. Hu X, Ma L, Zhang J, Li Z, Shen Y, Hu D. Use of pulmonary CT angiography with low tube voltage and low-iodine-concentration contrast agent to diagnose pulmonary embolism. *Sci Rep*. 2017;7(1):12741. doi:10.1038/s41598-017-13077-w
59. Hsieh J, Society of Photo-optical Instrumentation Engineers publisher. *Computed Tomography : Principles, Design, Artifacts, and Recent Advances*. Fourth edition. SPIE; 2022.
60. Barrett JF, Keat N. Artifacts in CT: Recognition and Avoidance. *RadioGraphics*. 2004;24(6):1679-1691. doi:10.1148/rg.246045065
61. Shih FY. *Image Processing and Pattern Recognition: Fundamentals and Techniques*. John Wiley & Sons; 2010.
62. Wang J, Fleischmann D. Improving spatial resolution at CT: development, benefits, and pitfalls. *Radiology*. 2018;289(1):261-262.
63. Dance DR, Christofides S, Maidment ADA, McLean ID, Ng KH. Diagnostic radiology physics: A handbook for teachers and students. Endorsed by: American Association of Physicists in Medicine, Asia-Oceania Federation of Organizations for Medical Physics, European Federation of Organisations for Medical Physics. Published online 2014.
64. Wright FW. *Radiology of the Chest and Related Conditions*. CRC Press; 2001.
65. Sudhyadhom A. On the molecular relationship between Hounsfield Unit (HU), mass density, and electron density in computed tomography (CT). *Plos one*. 2020;15(12):e0244861.

66. Gonzalez RC, Woods RE. Digital image processing, prentice hall. *Upper Saddle River, NJ*. Published online 2008.
67. Convolution. Accessed December 23, 2024. https://se.mathworks.com/discovery/convolution.html
68. Mildenberger P, Eichelberg M, Martin E. Introduction to the DICOM standard. *European radiology*. 2002;12(4):920-927.
69. Aiello M, Esposito G, Pagliari G, Borrelli P, Brancato V, Salvatore M. How does DICOM support big data management? Investigating its use in medical imaging community. *Insights into Imaging*. 2021;12(1):1-21.
70. Qi Y, Yang Z, Sun W, et al. A comprehensive overview of image enhancement techniques. *Archives of Computational Methods in Engineering*. Published online 2021:1-25.
71. Perona P, Malik J. Scale-space and edge detection using anisotropic diffusion. *IEEE Transactions on pattern analysis and machine intelligence*. 1990;12(7):629-639.
72. Yu-Qian Z, Wei-Hua G, Zhen-Cheng C, Jing-Tian T, Ling-Yun L. Medical images edge detection based on mathematical morphology. In: *2005 IEEE Engineering in Medicine and Biology 27th Annual Conference*. IEEE; 2006:6492-6495.
73. Lesage D, Angelini ED, Bloch I, Funka-Lea G. A review of 3D vessel lumen segmentation techniques: Models, features and extraction schemes. *Medical image analysis*. 2009;13(6):819-845.
74. Kahraman AT. *Automatic Interpretation of Lung CT Volume Images*.; 2017. Accessed December 6, 2024. https://urn.kb.se/rsolve?urn=urn:nbn:se:uu:diva-454689
75. He L, Ren X, Gao Q, Zhao X, Yao B, Chao Y. The connected-component labeling problem: A review of state-of-the-art algorithms. *Pattern Recognition*. 2017;70:25-43. doi:10.1016/j.patcog.2017.04.018
76. Chartrand G, Cheng PM, Vorontsov E, et al. Deep learning: a primer for radiologists. *Radiographics*. 2017;37(7):2113-2131.
77. Krohn J, Beyleveld G, Bassens A. *Deep Learning Illustrated: A Visual, Interactive Guide to Artificial Intelligence*. Addison-Wesley Professional; 2019.
78. Cheng PM, Montagnon E, Yamashita R, et al. Deep Learning: An Update for Radiologists. *RadioGraphics*. 2021;41(5):1427-1445.
79. Siddique N, Paheding S, Elkin CP, Devabhaktuni V. U-Net and Its Variants for Medical Image Segmentation: A Review of Theory and Applications. *IEEE Access*. 2021;9:82031-82057. doi:10.1109/ACCESS.2021.3086020
80. Lecun Y, Bottou L, Bengio Y, Haffner P. Gradient-based learning applied to document recognition. *Proc IEEE*. 1998;86(11):2278-2324. doi:10.1109/5.726791
81. El-Sawy A, EL-Bakry H, Loey M. CNN for Handwritten Arabic Digits Recognition Based on LeNet-5. In: Hassanien AE, Shaalan K, Gaber T, Azar AT, Tolba MF, eds. *Proceedings of the International Conference on Advanced Intelligent Systems and Informatics 2016*. Vol 533. Advances in Intelligent Systems and Computing. Springer International Publishing; 2017:566-575. doi:10.1007/978-3-319-48308-5_54
82. Krizhevsky A, Sutskever I, Hinton GE. ImageNet classification with deep convolutional neural networks. *Commun ACM*. 2017;60(6):84-90. doi:10.1145/3065386
83. Simonyan K, Zisserman A. Very deep convolutional networks for large-scale image recognition. *arXiv preprint arXiv:14091556*. Published online 2014.

84. Zhu YC, Jin PF, Bao J, Jiang Q, Wang X. Thyroid ultrasound image classification using a convolutional neural network. *Ann Transl Med*. 2021;9(20):1526-1526. doi:10.21037/atm-21-4328
85. Szegedy C, Liu W, Jia Y, et al. Going deeper with convolutions. In: *Proceedings of the IEEE Conference on Computer Vision and Pattern Recognition*. ; 2015:1-9.
86. Ma L, Wu H, Samundeeswari P. GoogLeNet-AL: A fully automated adaptive model for lung cancer detection. *Pattern Recognition*. 2024;155:110657. doi:10.1016/j.patcog.2024.110657
87. He K, Zhang X, Ren S, Sun J. Deep Residual Learning for Image Recognition. Published online 2015. doi:10.48550/ARXIV.1512.03385
88. He F, Liu T, Tao D. Why ResNet Works? Residuals Generalize. *IEEE Trans Neural Netw Learning Syst*. 2020;31(12):5349-5362. doi:10.1109/TNNLS.2020.2966319
89. Huang G, Liu Z, van der Maaten L, Weinberger KQ. Densely Connected Convolutional Networks. In: ; 2017:4700-4708. Accessed December 18, 2024. https://openaccess.thecvf.com/content_cvpr_2017/html/Huang_Densely_Connected_Convolutional_CVPR_2017_paper.html
90. Tan M, Le Q. Efficientnet: Rethinking model scaling for convolutional neural networks. In: *International Conference on Machine Learning*. PMLR; 2019:6105-6114. Accessed December 18, 2024. http://proceedings.mlr.press/v97/tan19a.html?ref=jina-ai-gmbh.ghost.io
91. Bai HX, Wang R, Xiong Z, et al. Artificial Intelligence Augmentation of Radiologist Performance in Distinguishing COVID-19 from Pneumonia of Other Origin at Chest CT. *Radiology*. 2020;296(3):E156-E165. doi:10.1148/radiol.2020201491
92. Howard AG, Zhu M, Chen B, et al. MobileNets: Efficient Convolutional Neural Networks for Mobile Vision Applications. Published online 2017. doi:10.48550/ARXIV.1704.04861
93. Qin D, Leichner C, Delakis M, et al. MobileNetV4: Universal Models for the Mobile Ecosystem. In: Leonardis A, Ricci E, Roth S, Russakovsky O, Sattler T, Varol G, eds. *Computer Vision – ECCV 2024*. Vol 15098. Lecture Notes in Computer Science. Springer Nature Switzerland; 2025:78-96. doi:10.1007/978-3-031-73661-2_5
94. Redmon J. You only look once: Unified, real-time object detection. In: *Proceedings of the IEEE Conference on Computer Vision and Pattern Recognition*. ; 2016. Accessed December 18, 2024. https://www.academis.eu/machine_learning/_downloads/51a67e9194f116abefff5192f683e3d8/yolo.pdf
95. Jiang P, Ergu D, Liu F, Cai Y, Ma B. A Review of Yolo algorithm developments. *Procedia computer science*. 2022;199:1066-1073.
96. Terven J, Córdova-Esparza DM, Romero-González JA. A comprehensive review of yolo architectures in computer vision: From yolov1 to yolov8 and yolo-nas. *Machine Learning and Knowledge Extraction*. 2023;5(4):1680-1716.
97. Girshick R, Donahue J, Darrell T, Malik J. Region-based convolutional networks for accurate object detection and segmentation. *IEEE transactions on pattern analysis and machine intelligence*. 2015;38(1):142-158.
98. Dai J, Li Y, He K, Sun J. R-fcn: Object detection via region-based fully convolutional networks. *Advances in neural information processing systems*. 2016;29. Accessed December 18, 2024. https://proceedings.neurips.cc/paper/2016/hash/577ef1154f3240ad5b9b413aa7346a1e-Abstract.html

99. Sabour S, Frosst N, Hinton GE. Dynamic Routing Between Capsules. In: *Advances in Neural Information Processing Systems*. Vol 30. Curran Associates, Inc.; 2017. Accessed December 18, 2024. https://proceedings.neurips.cc/paper_files/paper/2017/hash/2cad8fa47bbef282badbb8de5374b894-Abstract.html
100. Kwabena Patrick M, Felix Adekoya A, Abra Mighty A, Edward BY. Capsule Networks – A survey. *Journal of King Saud University - Computer and Information Sciences*. 2022;34(1):1295-1310. doi:10.1016/j.jksuci.2019.09.014
101. Goodfellow I, Pouget-Abadie J, Mirza M, et al. Generative Adversarial Nets. In: *Advances in Neural Information Processing Systems*. Vol 27. Curran Associates, Inc.; 2014. Accessed December 19, 2024. https://proceedings.neurips.cc/paper_files/paper/2014/hash/5ca3e9b122f61f8f06494c97b1afccf3-Abstract.html
102. Creswell A, White T, Dumoulin V, Arulkumaran K, Sengupta B, Bharath AA. Generative Adversarial Networks: An Overview. *IEEE Signal Process Mag*. 2018;35(1):53-65. doi:10.1109/MSP.2017.2765202
103. Goodfellow I, Pouget-Abadie J, Mirza M, et al. Generative adversarial networks. *Commun ACM*. 2020;63(11):139-144. doi:10.1145/3422622
104. Chen LC, Papandreou G, Kokkinos I, Murphy K, Yuille AL. DeepLab: Semantic Image Segmentation with Deep Convolutional Nets, Atrous Convolution, and Fully Connected CRFs. *IEEE Trans Pattern Anal Mach Intell*. 2018;40(4):834-848. doi:10.1109/TPAMI.2017.2699184
105. Chen LC, Zhu Y, Papandreou G, Schroff F, Adam H. Encoder-decoder with atrous separable convolution for semantic image segmentation. In: *Proceedings of the European Conference on Computer Vision (ECCV)*. ; 2018:801-818. Accessed December 18, 2024. http://openaccess.thecvf.com/content_ECCV_2018/html/Liang-Chieh_Chen_Encoder-Decoder_with_Atrous_ECCV_2018_paper.html
106. Iandola FN, Han S, Moskewicz MW, Ashraf K, Dally WJ, Keutzer K. SqueezeNet: AlexNet-level accuracy with 50x fewer parameters and <0.5MB model size. Published online 2016. doi:10.48550/ARXIV.1602.07360
107. Zhang X, Zhou X, Lin M, Sun J. Shufflenet: An extremely efficient convolutional neural network for mobile devices. In: *Proceedings of the IEEE Conference on Computer Vision and Pattern Recognition*. ; 2018:6848-6856. Accessed December 19, 2024. http://openaccess.thecvf.com/content_cvpr_2018/html/Zhang_ShuffleNet_An_Extremely_CVPR_2018_paper.html
108. Ma N, Zhang X, Zheng HT, Sun J. Shufflenet v2: Practical guidelines for efficient cnn architecture design. In: *Proceedings of the European Conference on Computer Vision (ECCV)*. ; 2018:116-131. Accessed December 19, 2024. http://openaccess.thecvf.com/content_ECCV_2018/html/Ningning_Lightweight_CNN_Architecture_ECCV_2018_paper.html
109. Zoph B, Vasudevan V, Shlens J, Le QV. Learning transferable architectures for scalable image recognition. In: *Proceedings of the IEEE Conference on Computer Vision and Pattern Recognition*. ; 2018:8697-8710. Accessed December 19, 2024. http://openaccess.thecvf.com/content_cvpr_2018/html/Zoph_Learning_Transferable_Architectures_CVPR_2018_paper.html
110. Dosovitskiy A. An image is worth 16x16 words: Transformers for image recognition at scale. *arXiv preprint arXiv:201011929*. Published online 2020. Accessed December 19, 2024. https://bibbase.org/service/mendeley/bfbbf840-4c42-3914-a463-19024f50b30c/file/264ac473-27b7-bd53-3963-f6a07df9b72e/Dosovitskiy_et_al___2021___An_Image_is_Worth_16x16_Words_Transformers_for_Im.pdf.pdf

111. Han K, Wang Y, Chen H, et al. A survey on vision transformer. *IEEE transactions on pattern analysis and machine intelligence*. 2022;45(1):87-110.
112. Liang M, Hu X. Recurrent convolutional neural network for object recognition. In: *Proceedings of the IEEE Conference on Computer Vision and Pattern Recognition*. ; 2015:3367-3375. Accessed December 19, 2024. http://openaccess.thecvf.com/content_cvpr_2015/html/Liang_Recurrent_Convolutional_Neural_2015_CVPR_paper.html
113. Wang J, Hu X. Convolutional neural networks with gated recurrent connections. *IEEE Transactions on Pattern Analysis and Machine Intelligence*. 2021;44(7):3421-3435.
114. Chen Y, Fan H, Xu B, et al. Drop an octave: Reducing spatial redundancy in convolutional neural networks with octave convolution. In: *Proceedings of the IEEE/CVF International Conference on Computer Vision*. ; 2019:3435-3444. Accessed December 19, 2024. http://openaccess.thecvf.com/content_ICCV_2019/html/Chen_Drop_an_Octave_Reducing_Spatial_Redundancy_in_Convolutional_Neural_Networks_ICCV_2019_paper.html
115. Jaderberg M, Simonyan K, Zisserman A, kavukcuoglu koray. Spatial Transformer Networks. In: *Advances in Neural Information Processing Systems*. Vol 28. Curran Associates, Inc.; 2015. Accessed December 19, 2024. https://proceedings.neurips.cc/paper_files/paper/2015/hash/33ceb07bf4eeb3da587e268d663aba1a-Abstract.html
116. Kirillov A, Mintun E, Ravi N, et al. Segment Anything. Published online 2023. doi:10.48550/ARXIV.2304.02643
117. Ma J, He Y, Li F, Han L, You C, Wang B. Segment anything in medical images. *Nat Commun*. 2024;15(1):654. doi:10.1038/s41467-024-44824-z
118. Long J, Shelhamer E, Darrell T. Fully convolutional networks for semantic segmentation. In: *Proceedings of the IEEE Conference on Computer Vision and Pattern Recognition*. ; 2015:3431-3440. Accessed December 19, 2024. http://openaccess.thecvf.com/content_cvpr_2015/html/Long_Fully_Convolutional_Networks_2015_CVPR_paper.html
119. Dolz J, Desrosiers C, Ben Ayed I. 3D fully convolutional networks for subcortical segmentation in MRI: A large-scale study. *NeuroImage*. 2018;170:456-470. doi:10.1016/j.neuroimage.2017.04.039
120. Kolesnikov A, Beyer L, Zhai X, et al. Big Transfer (BiT): General Visual Representation Learning. In: Vedaldi A, Bischof H, Brox T, Frahm JM, eds. *Computer Vision – ECCV 2020*. Vol 12350. Lecture Notes in Computer Science. Springer International Publishing; 2020:491-507. doi:10.1007/978-3-030-58558-7_29
121. Bishop CM, Bishop H. *Deep Learning: Foundations and Concepts*. Springer; 2024.
122. Goodfellow I, Bengio Y, Courville A. *Deep Learning*. MIT Press; 2016.
123. Gu J, Wang Z, Kuen J, et al. Recent advances in convolutional neural networks. *Pattern Recognition*. 2018;77:354-377. doi:10.1016/j.patcog.2017.10.013
124. Prince SJD (Simon JD. *Understanding Deep Learning*. Cambridge, Massachusetts; 2023.
125. Ronneberger O, Fischer P, Brox T. U-net: Convolutional networks for biomedical image segmentation. In: *International Conference on Medical Image Computing and Computer-Assisted Intervention*. Springer; 2015:234-241.
126. Azad R, Aghdam EK, Rauland A, et al. Medical Image Segmentation Review: The Success of U-Net. *IEEE Trans Pattern Anal Mach Intell*. 2024;46(12):10076-10095. doi:10.1109/TPAMI.2024.3435571

127. Wang R, Lei T, Cui R, Zhang B, Meng H, Nandi AK. Medical image segmentation using deep learning: A survey. *IET Image Processing*. 2022;16(5):1243-1267. doi:10.1049/ipr2.12419
128. Zhang Z, Liu Q, Wang Y. Road Extraction by Deep Residual U-Net. *IEEE Geosci Remote Sensing Lett*. 2018;15(5):749-753. doi:10.1109/LGRS.2018.2802944
129. Yuan X, Shi J, Gu L. A review of deep learning methods for semantic segmentation of remote sensing imagery. *Expert Systems with Applications*. 2021;169:114417. doi:10.1016/j.eswa.2020.114417
130. Isensee F, Jaeger PF, Kohl SAA, Petersen J, Maier-Hein KH. nnU-Net: a self-configuring method for deep learning-based biomedical image segmentation. *Nat Methods*. 2021;18(2):203-211. doi:10.1038/s41592-020-01008-z
131. Isensee F, Ulrich C, Wald T, Maier-Hein KH. Extending nnU-Net Is All You Need. In: Deserno TM, Handels H, Maier A, Maier-Hein K, Palm C, Tolxdorff T, eds. *Bildverarbeitung für die Medizin 2023*. Informatik aktuell. Springer Fachmedien Wiesbaden; 2023:12-17. doi:10.1007/978-3-658-41657-7_7
132. Isensee F, Jäger PF, Full PM, Vollmuth P, Maier-Hein KH. nnU-Net for Brain Tumor Segmentation. In: Crimi A, Bakas S, eds. *Brainlesion: Glioma, Multiple Sclerosis, Stroke and Traumatic Brain Injuries*. Vol 12659. Lecture Notes in Computer Science. Springer International Publishing; 2021:118-132. doi:10.1007/978-3-030-72087-2_11
133. Pettit RW, Marlatt BB, Corr SJ, Havelka J, Rana A. nnU-Net Deep Learning Method for Segmenting Parenchyma and Determining Liver Volume From Computed Tomography Images. *Annals of Surgery Open*. 2022;3(2):e155. doi:10.1097/AS9.0000000000000155
134. Ferrante M, Rinaldi L, Botta F, et al. Application of nnU-Net for Automatic Segmentation of Lung Lesions on CT Images and Its Implication for Radiomic Models. *JCM*. 2022;11(24):7334. doi:10.3390/jcm11247334
135. El-Taraboulsi J, Cabrera CP, Roney C, Aung N. Deep neural network architectures for cardiac image segmentation. *Artificial Intelligence in the Life Sciences*. 2023;4:100083. doi:10.1016/j.ailsci.2023.100083
136. Isensee F, Wald T, Ulrich C, et al. nnU-Net Revisited: A Call for Rigorous Validation in 3D Medical Image Segmentation. In: Linguraru MG, Dou Q, Feragen A, et al., eds. *Medical Image Computing and Computer Assisted Intervention – MICCAI 2024*. Vol 15009. Lecture Notes in Computer Science. Springer Nature Switzerland; 2024:488-498. doi:10.1007/978-3-031-72114-4_47
137. Rubin GD, Leipsic J, Schoepf UJ, Fleischmann D, Napel S. CT angiography after 20 years: a transformation in cardiovascular disease characterization continues to advance. *Radiology*. 2014;271(3):633-652.
138. Schönfeld T, Seitz P, Krieghoff C, et al. High-pitch CT pulmonary angiography (CTPA) with ultra-low contrast medium volume for the detection of pulmonary embolism: a comparison with standard CTPA. *Eur Radiol*. 2023;34(3):1921-1931. doi:10.1007/s00330-023-10101-8
139. Li Y, Cao G ying, Jing W zhan, Liu J, Liu M. Global trends and regional differences in incidence and mortality of cardiovascular disease, 1990−2019: findings from 2019 global burden of disease study. *European Journal of Preventive Cardiology*. 2023;30(3):276-286. doi:10.1093/eurjpc/zwac285
140. Baeßler B, Engelhardt S, Hekalo A, et al. Perfect Match: Radiomics and Artificial Intelligence in Cardiac Imaging. *Circ: Cardiovascular Imaging*. 2024;17(6). doi:10.1161/CIRCIMAGING.123.015490

141. Fusco R, Granata V, Grazzini G, et al. Radiomics in medical imaging: pitfalls and challenges in clinical management. *Jpn J Radiol*. 2022;40(9):919-929. doi:10.1007/s11604-022-01271-4
142. Kolossváry M, Kellermayer M, Merkely B, Maurovich-Horvat P. Cardiac Computed Tomography Radiomics: A Comprehensive Review on Radiomic Techniques. *Journal of Thoracic Imaging*. 2018;33(1):26-34. doi:10.1097/RTI.0000000000000268
143. Hrdlicka J, Jurka M, Bircakova B, et al. Even non-expert radiologists report chronic thromboembolic pulmonary hypertension (CTEPH) on CT pulmonary angiography with high sensitivity and almost perfect agreement. *Eur Radiol*. 2023;34(2):1086-1093. doi:10.1007/s00330-023-10098-0
144. Xu W, Deng M, Xi L, et al. Comparison of cardiovascular metrics on computed tomography pulmonary angiography of the updated and old diagnostic criteria for pulmonary hypertension in patients with chronic thromboembolic pulmonary hypertension. *Quant Imaging Med Surg*. 2023;13(12):7910-7923. doi:10.21037/qims-23-250
145. Aluja Jaramillo F, Gutierrez FR, Díaz Telli FG, Yevenes Aravena S, Javidan-Nejad C, Bhalla S. Approach to Pulmonary Hypertension: From CT to Clinical Diagnosis. *Radiographics*. 2018;38(2):357-373.
146. Aviram G, Shmueli H, Adam SZ, et al. Pulmonary Hypertension: A Nomogram Based on CT Pulmonary Angiographic Data for Prediction in Patients without Pulmonary Embolism. *Radiology*. 2015;277(1):236-246.
147. Mahammedi A, Oshmyansky A, Hassoun PM, Thiemann DR, Siegelman SS. Pulmonary artery measurements in pulmonary hypertension: the role of computed tomography. *J Thorac Imaging*. 2013;28(2):96-103.
148. Wu Jinlin, Zafar Mohammad A., Li Yupeng, et al. Ascending Aortic Length and Risk of Aortic Adverse Events. *J Am Coll Cardiol*. 2019;74(15):1883-1894.
149. Lavall D, Schäfers HJ, Böhm M, Laufs U. Aneurysms of the Ascending Aorta. *Dtsch Arztebl Int*. 2012;109(13):227-233.
150. Scarpato BM, Locke BW, Bledsoe J, et al. The association between pulmonary artery enlargement and mortality in an Emergency Department population undergoing computed tomography pulmonary angiography. *Pulm circ*. 2023;13(2):e12225. doi:10.1002/pul2.12225
151. Zhao W, Guo J, Dong N, Hei H, Duan X, Shen C. Diagnostic value of 3D volume measurement of central pulmonary artery based on CTPA images in the pulmonary hypertension. *BMC Med Imaging*. 2023;23(1):211. doi:10.1186/s12880-023-01180-6
152. Pienn M, Gertz RJ, Gerhardt F, et al. CT-derived lung vessel morphology correlates with prognostic markers in precapillary pulmonary hypertension. *The Journal of Heart and Lung Transplantation*. 2024;43(1):54-65. doi:10.1016/j.healun.2023.08.013
153. eCFR — Code of Federal Regulations. Accessed February 25, 2019. https://www.ecfr.gov/current/title-21/chapter-I/subchapter-J/part-1020#1020.33
154. Bae KT, Mody GN, Balfe DM, et al. CT Depiction of Pulmonary Emboli: Display Window Settings. *Radiology*. 2005;236(2):677-684.
155. Kang DK, Thilo C, Schoepf UJ, et al. CT signs of right ventricular dysfunction: prognostic role in acute pulmonary embolism. *J Am Coll Cardiol Img*. 2011;4(8):841-849.
156. Ecabert O, Peters J, Walker MJ, et al. Segmentation of the heart and great vessels in CT images using a model-based adaptation framework. *Medical Image Analysis*. 2011;15(6):863-876. doi:10.1016/j.media.2011.06.004

157. Moses D, Sammut C, Zrimec T. Automatic segmentation and analysis of the main pulmonary artery on standard post-contrast CT studies using iterative erosion and dilation. *Int J CARS*. 2016;11(3):381-395. doi:10.1007/s11548-015-1265-3
158. Zhuang X, Bai W, Song J, et al. Multiatlas whole heart segmentation of CT data using conditional entropy for atlas ranking and selection. *Medical Physics*. 2015;42(7):3822-3833. doi:10.1118/1.4921366
159. Baskaran L, Al'Aref SJ, Maliakal G, et al. Automatic segmentation of multiple cardiovascular structures from cardiac computed tomography angiography images using deep learning. Zirlik A, ed. *PLoS ONE*. 2020;15(5):e0232573. doi:10.1371/journal.pone.0232573
160. Koo HJ, Lee JG, Lee JB, Kang JW, Yang DH. Deep Learning Based Automatic Segmentation of the Thoracic Aorta from Chest Computed Tomography in Healthy Korean Adults. *European Journal of Vascular and Endovascular Surgery*. Published online July 2024:S1078588424006427. doi:10.1016/j.ejvs.2024.07.030
161. Suzuki H, Kawata Y, Aokage K, et al. Aorta and main pulmonary artery segmentation using stacked U-Net and localization on non-contrast-enhanced computed tomography images. *Medical Physics*. 2024;51(2):1232-1243. doi:10.1002/mp.16654
162. Rivera-Lebron B, McDaniel M, Ahrar K, et al. Diagnosis, Treatment and Follow Up of Acute Pulmonary Embolism: Consensus Practice from the PERT Consortium. *Clin Appl Thromb Hemost*. 2019;25:107602961985303. doi:10.1177/1076029619853037
163. Özkan H, Osman O, Şahin S, Boz AF. A novel method for pulmonary embolism detection in CTA images. *Computer Methods and Programs in Biomedicine*. 2014;113(3):757-766. doi:10.1016/j.cmpb.2013.12.014
164. Zhou C, Chan HP, Hadjiiski LM, et al. Automated detection of pulmonary embolism (PE) in computed tomographic pulmonary angiographic (CTPA) images: multiscale hierachical expectation-maximization segmentation of vessels and PEs. In: Giger ML, Karssemeijer N, eds. ; 2007:65142F. doi:10.1117/12.713769
165. Myers MH, Beliaev I, Lin KI. Machine Learning Techniques in Detecting of Pulmonary Embolisms. In: *2007 International Joint Conference on Neural Networks*. IEEE; 2007:385-390. doi:10.1109/IJCNN.2007.4370987
166. Wang X, Song X, Chapman BE, Zheng B. Improving performance of computer-aided detection of pulmonary embolisms by incorporating a new pulmonary vascular-tree segmentation algorithm. In: van Ginneken B, Novak CL, eds. ; 2012:83152U. doi:10.1117/12.911301
167. Ozkan H, Tulum G, Osman O, Sahin S. Automatic Detection of Pulmonary Embolism in CTA Images Using Machine Learning. *ElAEE*. 2017;23(1):63-67. doi:10.5755/j01.eie.23.1.17585
168. Tajbakhsh N, Shin JY, Gotway MB, Liang J. Computer-aided detection and visualization of pulmonary embolism using a novel, compact, and discriminative image representation. *Medical Image Analysis*. 2019;58:101541. doi:10.1016/j.media.2019.101541
169. Rajan D, Beymer D, Abedin S, Dehghan E. Pi-PE: A Pipeline for Pulmonary Embolism Detection using Sparsely Annotated 3D CT Images. In: *Proceedings of the Machine Learning for Health NeurIPS Workshop*. PMLR; 2020:220-232. Accessed February 16, 2023. https://proceedings.mlr.press/v116/rajan20a.html

170. Weikert T, Winkel DJ, Bremerich J, et al. Automated detection of pulmonary embolism in CT pulmonary angiograms using an AI-powered algorithm. *Eur Radiol*. 2020;30(12):6545-6553. doi:10.1007/s00330-020-06998-0
171. Wolf I, Vetter M, Wegner I, et al. The Medical Imaging Interaction Toolkit. *Medical Image Analysis*. 2005;9(6):594-604. doi:10.1016/j.media.2005.04.005
172. Lambert Z, Petitjean C, Dubray B, Kuan S. SegTHOR: Segmentation of Thoracic Organs at Risk in CT images. In: *2020 Tenth International Conference on Image Processing Theory, Tools and Applications (IPTA)*. IEEE; 2020:1-6. doi:10.1109/IPTA50016.2020.9286453
173. Masoudi M, Pourreza HR, Saadatmand-Tarzjan M, Eftekhari N, Zargar FS, Rad MP. A new dataset of computed-tomography angiography images for computer-aided detection of pulmonary embolism. *Sci Data*. 2018;5(1):180180. doi:10.1038/sdata.2018.180
174. Colak E, Kitamura FC, Hobbs SB, et al. The RSNA Pulmonary Embolism CT Dataset. *Radiology: Artificial Intelligence*. 2021;3(2):e200254. doi:10.1148/ryai.2021200254
175. Pfeffer Y, Mayer A, Zholkover A, M.d EK. A system for automatic aorta sections measurements on chest CT. In: *Medical Imaging 2016: Computer-Aided Diagnosis*. Vol 9785. International Society for Optics and Photonics; 2016:978505.
176. López-Linares Román K, De La Bruere I, Onieva J, et al. 3D Pulmonary Artery Segmentation from CTA Scans Using Deep Learning with Realistic Data Augmentation. In: Stoyanov D, Taylor Z, Kainz B, et al., eds. *Image Analysis for Moving Organ, Breast, and Thoracic Images*. Vol 11040. Lecture Notes in Computer Science. Springer International Publishing; 2018:225-237. doi:10.1007/978-3-030-00946-5_23
177. Sharkey MJ, Taylor JC, Alabed S, et al. Fully automatic cardiac four chamber and great vessel segmentation on CT pulmonary angiography using deep learning. *Front Cardiovasc Med*. 2022;9:983859. doi:10.3389/fcvm.2022.983859
178. Wasserthal J, Breit HC, Meyer MT, et al. TotalSegmentator: Robust Segmentation of 104 Anatomic Structures in CT Images. *Radiology: Artificial Intelligence*. 2023;5(5):e230024. doi:10.1148/ryai.230024
179. Chettrit D, Bregman Amitai O, Tamir IA, Bar A, Elnekave E. PHT-bot: a deep learning based system for automatic risk stratification of COPD patients based upon signs of pulmonary hypertension. In: Hahn HK, Mori K, eds. *Medical Imaging 2019: Computer-Aided Diagnosis*. SPIE; 2019:23. doi:10.1117/12.2512469
180. Schneider J, Meske C, Kuss P. Foundation Models: A New Paradigm for Artificial Intelligence. *Bus Inf Syst Eng*. 2024;66(2):221-231. doi:10.1007/s12599-024-00851-0
181. Maizlin ZV, Vos PM, Godoy MB, Cooperberg PL. Computer-aided Detection of Pulmonary Embolism on CT Angiography: Initial Experience. *Journal of Thoracic Imaging*. 2007;22(4):324-329. doi:10.1097/RTI.0b013e31815b89ca
182. Wittenberg R, Berger FH, Peters JF, et al. Acute Pulmonary Embolism: Effect of a Computer-assisted Detection Prototype on Diagnosis—An Observer Study. *Radiology*. 2012;262(1):305-313. doi:10.1148/radiol.11110372
183. Lahiji K, Kligerman S, Jeudy J, White C. Improved Accuracy of Pulmonary Embolism Computer-Aided Detection Using Iterative Reconstruction Compared With Filtered Back Projection. *American Journal of Roentgenology*. 2014;203(4):763-771. doi:10.2214/AJR.13.11838

184. Tajbakhsh N, Gotway MB, Liang J. Computer-Aided Pulmonary Embolism Detection Using a Novel Vessel-Aligned Multi-planar Image Representation and Convolutional Neural Networks. In: Navab N, Hornegger J, Wells WM, Frangi A, eds. *Medical Image Computing and Computer-Assisted Intervention -- MICCAI 2015*. Vol 9350. Lecture Notes in Computer Science. Springer International Publishing; 2015:62-69. doi:10.1007/978-3-319-24571-3_8
185. Huang SC, Kothari T, Banerjee I, et al. PENet—a scalable deep-learning model for automated diagnosis of pulmonary embolism using volumetric CT imaging. *npj Digit Med*. 2020;3(1):61. doi:10.1038/s41746-020-0266-y
186. Mohamad-Djafari A. *Inverse Problems in Vision and 3D Tomography*. John Wiley & Sons; 2013.
187. Adler J, Öktem O. Solving ill-posed inverse problems using iterative deep neural networks. *Inverse Problems*. 2017;33(12):124007. doi:10.1088/1361-6420/aa9581
188. Gonzalez G, Jimenez-Carretero D, Rodriguez-Lopez S, et al. Automated axial right ventricle to left ventricle diameter ratio computation in computed tomography pulmonary angiography. *PLoS One*. 2015;10(5):e0127797.
189. Melzig C, Do TD, Egenlauf B, et al. Diagnostic accuracy of automated 3D volumetry of cardiac chambers by CT pulmonary angiography for identification of pulmonary hypertension due to left heart disease. *Eur Radiol*. 2022;32(8):5222-5232. doi:10.1007/s00330-022-08663-0
190. Zantonelli G, Cozzi D, Bindi A, et al. Acute Pulmonary Embolism: Prognostic Role of Computed Tomography Pulmonary Angiography (CTPA). *Tomography*. 2022;8(1):529-539. doi:10.3390/tomography8010042
191. Khan S, Naseer M, Hayat M, Zamir SW, Khan FS, Shah M. Transformers in Vision: A Survey. *ACM Comput Surv*. 2022;54(10s):1-41. doi:10.1145/3505244
192. Liu Z, Wang Y, Vaidya S, et al. KAN: Kolmogorov-Arnold Networks. Published online June 16, 2024. doi:10.48550/arXiv.2404.19756